New Strategies for Defect Passivation in High-Efficiency Perovskite Solar Cells

Seckin Akin, Neha Arora, Shaik M. Zakeeruddin, Michael Grätzel, Richard H. Friend, M. Ibrahim Dar**

Dr. N. Arora, Dr. M. I. Dar, Prof. R. H. Friend
Cavendish Laboratory, Department of Physics, University of Cambridge, JJ Thomson Avenue, Cambridge CB3 0HE, UK
E-mail: id338@cam.ac.uk, na498@cam.ac.uk

Dr. S. Akin, Dr. S. M. Zakerruddin, Prof. M. Grätzel
Laboratory of Photonics and Interfaces, Department of Chemistry and Chemical Engineering, École Polytechnique Fédérale de Lausanne, Lausanne CH-1015, Switzerland

Dr. S. Akin
Department of Metallurgical and Materials Engineering, Karamanoglu Mehmetbey University, 70100, Karaman, Turkey

Keywords: (perovskite solar cells, defects, passivation, efficiency, mixed-cation-halide, 2D-3D, engineering, stability)

Lead halide perovskite solar cells (PSCs) now show excellent efficiencies and encouraging levels of stability. Further improvements in performance require better control of electron-hole recombination processes associated with trap states. Such trap states are considered to be associated with vacancies and defects at crystallite surfaces. We consider here how these traps can be mitigated by improving the quality of the perovskite layer and interfaces in fully assembled device configurations. In this review, we discuss most recent design strategies reported in the literature, that have been explored to tune grain orientation, to passivate defects, and to improve charge-carrier lifetimes. Specifically, we discuss advances made with single-cation, mixed-cation, and mixed-halide, and three-dimensional/two-dimensional-(3D/2D) bilayer based light absorbers. We focus on interfacial, compositional, and band alignment engineering with their consequent effects on the open-circuit voltage, power conversion efficiency, and stability.

1. Introduction

The impetus to commercialize lead-halide perovskite solar cells (PSCs) as next-generation solar cells arises from their simple and facile solution-processibility.[1,2,3,4,5] In addition, their desired optoelectronic properties such as high absorption coefficient with long carrier diffusion lengths have promoted the research domain targeting low-cost and high-efficiency solar cells. [6,7,8,9] Initially, Miyasaka and co-workers reported breakthrough research on liquid electrolyte based PSCs with power conversion efficiency (*PCE*) of 3.8% in 2008.[10] Subsequently, higher *PCEs* were obtained while employing spiro-OMeTAD, a solid-state hole conductor in PSCs.[4,6] All-solid-state PSCs also revealed that the generation of free-charges inside the bulk of the perovskite absorber layer. Since then, the PSC research field has expanded dramatically with *PCE*s exceeding 25%.[11] One of the important aspects of improving the *PCE* of PSCs is to minimize non-radiative recombination processes and preclude the carrier quenching both within the photoactive layer and at the interfaces while simultaneously promoting balanced charge transport and collection.[12,13,14,15]

Although it is difficult to know the nature of defects and to differentiate defects located at the surface and grain boundaries (GBs), their formation could be finely controlled by controlling the growth and morphology of the perovskite films and other structures.[16,17,18] In addition, the compositional engineering of these ABX_3 compounds, which allows tailoring of the bandgap, could be explored to improve the optoelectronic properties with great rationality to simultaneously increase the efficiency and stability of PSCs. Recently, many advances in the compositional (cation and/or anion) engineering including the partial substitution of formamidinium (FA^+) cation and I^-, respectively, with methylammonium (MA^+) and Br^- have been made to enhance both performance and stability.[19,20] In addition, both organic and inorganic cations like cesium (Cs^+), rubidium (Rb^+), potassium (K^+), sodium

(Na^+), silver (Ag^+), guanidinium (Gua^+) have been explored into the perovskite films to enhance the photovoltage (V_{OC}) of PSCs.[21,22,23,24]

The mitigation of instability issues, which get aggravated in the presence of traps, is one of the main challenges that PSCs technology is facing currently. Therefore, it has become imperative to passivate defects located at the surface and GBs.[25,26] Towards this end, various strategies such as interface engineering via surface passivation and charge compensation by using metal oxides, additive engineering approach, which was employed to enlarge the dimensions of perovskite grains, and to increase the crystallinity, and small molecules, or polymers etc. have been developed for the stabilization of crystal phase and defect management in PSCs. [27,28,29] More recently, the application of 2D Ruddlesden–Popper layered perovskites $(RNH_3)_2(A)_{n-1}BX_{3n+1}$), ($n$ = 1, 2, 3, 4,. . ∞) (where n is the number of layers and RNH_3 are large alkyl ammonium cations) have been proposed as stable alternatives to 3D perovskites because of their superior hydrophobicity and thermostability.[1, 30,31] However, the PSCs employing 2D perovskites as the active layer display relatively poor performances primarily due to the anisotropic transport properties, which are intrinsically associated with the layered structure. Interestingly, in conjugation with the 3D perovskites, both efficiency and stability can be synergistically improved mainly due to the passivation of interfacial GBs in a 3D/2D bilayer configuration.[1] Such a bilayer architecture also minimizes the issues associated with the hygroscopic nature of the 3D-perovskite material and sensitivity towards high temperature, which can induce the degradation of the interfaces and rapidly decrease the photovoltaic performances within a short period of operation. The graded combination of 2D/3D can also hinder the ionic-motion and mitigate the parasitic interfacial charge-carrier recombination.[32]

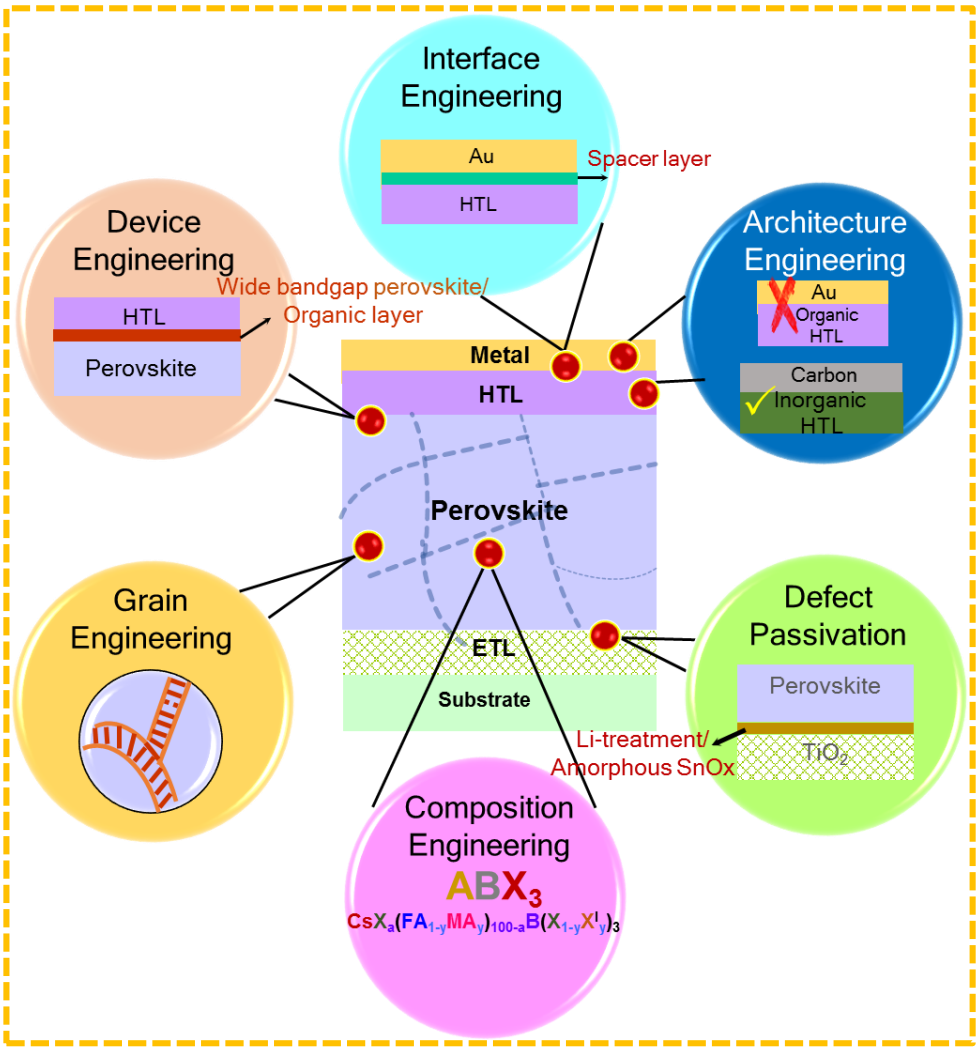

Figure 1. Schematic illustration of different passivation strategies for high-efficiency perovskite solar cells.

In this review, we provide an overview of the recent progress on the strategies adopted to passivate defects to realize high-efficiency PSCs (**Figure 1**). Firstly, we aim to highlight the routes that have been successfully explored to control the non-radiative recombination and enhance the photovoltage of PSCs. Specifically, most recent reports on PSCs based on single-cation to mixed-cation and/or mixed- halide to the 3D/2D perovskite system will be discussed. The next section illustrates the stability of the PSCs based on these systems probed under illumination, humid conditions and thermal stress. Finally, the last section will provide the perspectives about this enticing scientific domain, i.e., defect passivation in PSCs.

2. Single cation-based perovskites

In the last decade, PSCs has become a promising and emerging technology with certified efficiency exceeding 25%,[11] This photovoltaic technology began with PSCs involving single-cation based light absorber with an efficiency of 3.8%.[10] The forthcoming sections highlight recent reports showing that the approaches including composition-additive, charge transport layers, interface, and device architecture engineering are critical to the performance of these single cation-based PSCs.

2.1. Composition-additive engineering in single cation perovskites

A high-quality perovskite film with low-amount of grain boundaries and fewer trap states in the bulk and/or at the interfaces is necessary to obtain good performance. Composition-additive engineering is one of the most efficient strategies to obtain perovskite films with high crystallinity, smooth surfaces, and large grains, which reduce the grain boundaries and trap states. In this section, composition-additive engineering approaches for single-cation perovskite absorber are discussed.

Carmano *et al*. fabricated the n-i-p-type mesoporous PSCs based on a non-stoichiometric PbI_2: MAI ratio (x: 1, being $x \geq 1$) in the perovskite precursor solution.[33] The obtained results demonstrated that the unreacted PbI_2 enhances the crystallinity of the perovskite film due to the stronger interfacial coupling at the interface and promotes the electron transfer from perovskite to TiO_2 layer owing to better band alignment. As a result of these remarkable properties, an improvement in the *FF* and V_{OC} (as high as 1.11 V) was acquired, boosting the averaged *PCE* from 16.2% to values close to 18%, with a champion efficiency of >19%. It is worth mentioning that the concept of using excess PbI_2 renders the use of precursors containing a stoichiometric ratio of PbI_2: MAI undesired, as was commonly believed in the PSC field. In some cases, different methodologies were introduced to induce rapid crystallization of the perovskite structures with a slight excess of PbI_2. For example,

laser irradiation was explored to obtain homogeneous and dense-grained $MAPbI_3$ films.[34] The advantage of laser irradiation is to produce a thermal gradient, which was found to be beneficial for the formation of the desired amount of PbI_2 on the surface of $CH_3NH_3PbI_3$ perovskite film. Consequently, the parasitic recombination occurring at the interface decreased due to self-passivation, minimizing the voltage loss to 0.41 V.

New molecules were also designed to passivate the defects (defect-healing), which greatly improved the efficiency and stability of PSCs. Zheng *et al*. reported a study to passivate the ionic defects at the surfaces and grain boundaries of $MAPbI_3$ perovskite films by using quaternary ammonium halides (QAHs), i.e., $NR_4^+X^-$(R is an alkyl or aryl group and X is halide).[35] In addition to a significant reduction in the trap-state density, an improvement in the charge carrier lifetime was also observed in the presence of choline chloride-based passivation layer as shown in **Figure 2a**. As a result of successful passivation of ionic defects, the V_{OC} of the p-i-n-architecture based planar devices increased from 1.04 V to 1.15 V with a significant enhancement in *PCE* (17.1% to 20.0%) and hysteresis-free behavior. In addition, the defect healing approach enhanced the ambient stability of the perovskite films. The larger V_{OC} yielded by the devices involving choline chloride QAHs was attributed to their zwitterionic structure and to the additional passivation effects of the halide ions (**Figure 2b**). Another interesting aspect related to additive engineering approach is to achieve high-quality perovskite absorber films. For example, Wu *et al*. demonstrated that the addition of a small amount of H_2O into PbI_2/DMF makes a homogenous precursor solution for depositing high-quality PbI_2 film in a two-step method.[36] Apparently, moisture can assist the grain growth of the perovskite film to improve the charge-carrier lifetime and carrier mobility.[37] In this study, highly pure, smooth, crystalline and oriented perovskite films were deposited on PEDOT:PSS surface. The PbI_2 film involving 2 wt% water exhibited the smoothest and

densely packed films composed of large grains. The inverted-type champion PSC showed a remarkable *FF* of 0.85, resulting in a *PCE* of 18% with a V_{OC} of 1.03 V.

Recently Han *et al*. developed an additive-based room temperature process to obtain high-quality $MAPbI_3$ films with micron-sized grains (>2 μm), employing a simple low-vacuum process.[38] Authors used methylammonium thiocyanate (MASCN) as an additive and achieved microsecond-range carrier lifetimes and highly crystalline perovskite films at room temperature. As a result of these excellent film characteristics, the best *PCE* of 18.22% (average 16.92%) with low hysteresis and respectable environmental stability under the standard illumination was realized, whereas the control device (without additive) demonstrated only 2.04% *PCE* with J_{SC} of 8.78 mA cm^{-2}, V_{OC} of 0.638 V and *FF* of 0.36, under similar conditions. Such an improvement in the photovoltaic parameters was explained on the basis of increased grain size and improved crystallinity of perovskite films. The additive-based mechanism was proposed and verified by Tindall-effect tests and DLS measurements. The coordination of SCN^- with Pb^{2+} facilitates enlargement of the precursor aggregates up to microscale before spin coating which arranges in an ordered fashion on the substrates during the film deposition. The solvent and volatile SCN^- were removed by applying low-vacuum as depicted in **Figure 2c**.

Very recently, Zhou *et al*. employed the imidazole sulfonate zwitterion, 4-(1H-imidazol-3-ium-3-yl) butane-1-sulfonate (IMS), as a bifunctional additive in an n-i-p planar $MAPbI_3$ based type PSCs.[39] It was reported that this additive not merely arranges the crystal orientation but also passivates the trap states of $MAPbI_3$ perovskite film especially the iodine vacancy. The effect of bi-functional IMS additive observed due to coordination between sulfonate moiety of IMS and Pb^{2+} ion as well as electrostatic interaction between imidazole of IMS and I^- ion of perovskite (**Figure 2d**). As a result, the *PCE* and *Voc* increased from 18.77% and 1.10 V to 20.84% and 1.14 V, respectively, while hysteresis decreased in the

presence of 0.5 wt% IMS doping. For a 1.2 wt% IMS doping ratio, a V_{OC} of 1.208 V was achieved, and this was claimed to be the highest V_{OC} for $MAPbI_3$ employing n-i-p structured planar PSCs.

A record V_{OC} of 1.26 V has been demonstrated for planar solar cells with inverted architecture based on smooth $MAPbI_3$ perovskite films with large grains.[40] The perovskite films were obtained after employing the combination of lead acetate ($PbAc_2$) and lead chloride ($PbCl_2$) precursors and optimizing the contact layers. In addition, exceptionally long photoluminescence lifetimes, which translated into a magnificent *PCE* of ~20.7% were reported.

In addition to the molecular doping, the introduction of metal ions in the perovskite structure is another promising approach to address the main critical concerns of PSCs. Towards this end, various monovalent cations including Na^+, Ag^+, Cu^+ were introduced in the $MAPbI_3$ films to improve the optoelectronic properties of $MAPbI_3$ structures, [41,42] which consequently increased the photovoltaic performance of the resulting devices. The role of other inorganic cations such as Cs^+ and Rb^+ was also investigated in various perovskite compositions and the insights gained through various structural, thermal and spectroscopic studies amply established the absence of Rb^+ whereas, under similar conditions, a certain amount of Cs^+ was found to be occupying the A-site in 3D perovskite.[43] In another interesting study, Pb metal in $MAPbI_3$ perovskite films was substituted by nine different alternative divalent metal species such as Co, Cu, Fe, Mg, Mn, Ni, Sn, Sr, Zn to screen the tolerance of perovskite film towards extrinsic homovalent metal species and its impact on the photovoltaic performance of inverted-type $MAPbI_3$ PSCs.[44] It was proven that the $MAPbI_3$ film shows a much higher tolerance without any performance loss in comparison to crystalline silicon when less than 3% of the Pb^{2+} ions were replaced. This compositional engineering approach also showed that not only well-known Sn^{2+} but also Co^{2+} can replace Pb^{2+} from the

perovskite lattice as revealed by the crystallographic analysis. By using the optimum molar ratio of 63Pb:1Co, the best *PCE* of 17.2% with an improved V_{OC} (from 0.96 V for the baseline to 1.05 V for 63Pb:1Co and to 1.08 V for 31Pb:1Co ratio) over the standard $MAPbI_3$. The ~120 mV increase in V_{OC} was attributed to the ability of Co^{2+} to shift the Fermi level and valence band edge of the perovskite material into a more favourable energetic alignment with HTL. Apparently, the obtained results showed that transition metal substitution could provide a new dimension for tuning the electronic and crystallographic properties of perovskite films while maintaining high photovoltaic performance.

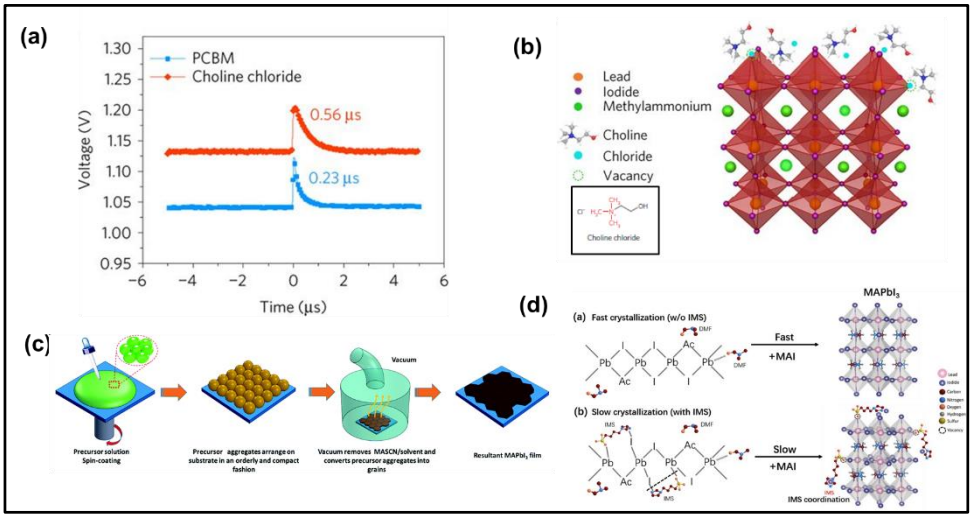

Figure 2. a) Charge carrier lifetime curves of control and choline chloride-treated devices, estimated from transient photovoltage measurement under open-circuit conditions. Reproduced with permission. [35] Copyright 2017, Nature Publishing Group. **b)** Schematic illustration of quaternary ammonium halides assembled on the defect sites (the red and blue symbols represent the N and O atoms of the choline chloride molecule, respectively). Reproduced with permission.[35] Copyright 2017, Nature Publishing Group. **c)** Schematic flow diagram of the room-temperature process to deposit $MAPbI_3$ films and proposed film formation mechanism. Reproduced with permission.[38] Copyright 2017, Royal Society of Chemistry. **d)** Proposed formation mechanisms of $MAPbI_3$ perovskite structure a) without and b) with imidazole sulfonate zwitterion, 4-(1H-imidazol-3-ium-3-yl)butane-1-sulfonate (IMS), as a bifunctional additive. Reproduced with permission.[39] Copyright 2019, John Wiley & Sons.

In this section, we have covered recent reports of photovoltage enhancement in single-cation based PSCs in the context of composition-additive engineering. Quiet versatile

methods have been discussed including defect healing, increase in grain size and introduction of metal ions in the perovskite absorber. In the following, the different methods for energy band-alignment and interface engineering resulting in the improvement of photovoltaic parameters will be discussed.

2.2. ETL engineering in single cation perovskites

The electron transport layers (ETLs) play an indispensable role in PSCs owing to their key electron extracting/transporting features. Although TiO_2 is considered as the most promising ETL material for highly efficient PSCs, it needs to be modified using suitable approaches or replaced with better alternatives to combat the current challenges, i.e., low electron mobility, insufficient band-offset, and high sintering temperature. In this section, highly promising modification methods and alternative ETL materials are presented to illustrate the importance of ETL materials in the state-of-the-art PSCs based on the single-cation absorber.

The impact of magical $TiCl_4$ treatment was unraveled using photothermal deflection spectroscopy (PDS), and results amply showed a decrease in the energetic disorder not merely in mesoporous TiO_2 but also in $CH_3NH_3PbI_3$ light absorber layer.[45] Using [6,6]-phenyl-C_{61}-butyric acid (PCBA) monolayer modified compact TiO_2 (c-TiO_2) substrates, high-quality $CH_3NH_3PbI_3$ films were deposited for planar heterojunction PSCs.[46] The PCBA interfacial layer reduced the hole recombination by acting as the hole blocking layer at the c-TiO_2/$CH_3NH_3PbI_3$ interface and facilitating efficient electron extraction by the ETL. The formation of a chemical bond between c-TiO_2 and the carboxyl group of PCBA as well as the low solubility of PCBA in perovskite solvent of N, N-dimethylformamide (DMF) helped to obtain pin-hole free perovskite films, resulting in significant enhancement of photovoltaic performance from 7.46% to 13.33%. The best *PCE* of 17.76% with an outstanding V_{OC} of 1.16 V was achieved by optimizing the perovskite thickness.

Miyasaka and co-workers developed a fully low-temperature-processed PSCs employing an ultrathin amorphous TiO_x ETL in combination with brookite TiO_2 prepared at <150 °C.[47] The TiO_x/brookite TiO_2 bilayer ETL based PSCs demonstrated an excellent *PCE* up to 21.6%, supported by a remarkable V_{OC} and *FF* of 1.18 V and 0.83, respectively, as a result of well-matched band alignment with respect to brookite TiO_2. The authors also examined SnO_x as an alternative ETL to TiO_x in combination with brookite TiO_2. Although the SnO_x/brookite TiO_2 bilayer ETL based PSCs yielded V_{OC} and J_{SC} as high as TiO_x/brookite TiO_2 based PSCs, loss of *FF* resulted in relatively lower *PCE*. The electron band edge potentials of ETLs and brookite TiO_2 were evoked to explain the drop in *FF*, whereas more negative conduction band edge of SnO_x exhibited an energy barrier for electron injection from brookite TiO_2 into SnO_x layer.

In comparison to TiO_2 and SnO_2, ZnO exhibits more promising electron extraction ability owing to its superior electron mobility and more favourable band-offset. A simple strategy was developed to obtain planar PSCs at low-temperature by combining bi-functional self-assembled monolayer (SAM)-modified ZnO electron-accepting layers with sequentially prepared perovskite active layers.[48] Highly polar molecules of bithiophene conjugated cyanoacrylic acid (T2CA) julolidine moiety conjugated cyanoacrylic acid (JTCA) were employed as the SAM as shown in **Figure 3a**. The JTCA-modified ZnO ETL based PSCs reached a *PCE* of 18.82% with V_{OC} of 1.13 V, whereas the pristine ZnO ETL based PSC reached only 15.41% with V_{OC} of 1.06 V. The trap state measurements showed a lower trap density in the JTCA (SAM)-modified device whereas the carrier mobility of the ITO-JTCA employing device was 50% higher (0.61 $cm^2\ V^{-1}\ s^{-1}$) than that of bare ITO (0.43 $cm^2\ V^{-1}\ s^{-1}$). A large enhancement in the V_{OC} from 0.962 V to 1.135 V and *PCE* from 14.15% to 19.14% was reported for PEDOT:PSS HTL based inverted type $MAPbI_3$ based PSCs by employing two-dimensional (2D) materials such as graphene oxide (GO) at PEDOT: PSS/perovskite

interface and MoS_2 at PCBM/Ag interface.[49] The V_{OC} was further improved to 1.176 V when the perovskite structure was doped with Br^- ($MAPbI_{2.5}Br_{0.5}$). In addition to enhanced ohmic contact, which facilitates the rapid transfer of the electrons across the MoS_2/Ag interface, MoS_2 layer also showed a hole blocking potential to decrease the recombination at the interface near the cathode. The combination of energy level matching at the contact interface and the electronic and chemical properties of the 2D materials resulted in the improvement of photovoltaic parameters. The enhancement in the device stability was also reported in the presence of interlayers due to the blocking of the ion diffusion at the PEDOT: PSS/perovskite and PCBM/Ag interfaces.

More recently, a hydrophobic fullerene derivative, [6,6]-phenyl-C61-butyric acid-N,N-dimethyl-3-(2-thienyl)propanam ester (PCBB-S-N) containing a functional sulphur atom and C_{60} was synthesized and employed as an intermediary layer on PCBM ETL to heal the defect states in PSCs (**Figure 3b**).[50] The resulting planar p-i-n $MAPbI_3$ PSCs exhibited much-improved *PCE* of over 21% relative to bare PCBM ETL-based control device (*PCE* 17.41%), and also showed excellent moisture and thermal stability. The enhanced V_{OC} of 70 mV was attributed to the slightly increased LUMO energy level of PCBB-S-N and passivation of antisite defects by the pendent thiophene moieties, while higher *FF* and J_{SC} values were explained on the basis of formation of compact and homogeneous PCBB-S-N film contributing to its electronic contact with the cathode.

2.3. HTL engineering in single cation perovskites

Despite playing a key role in PSCs, the high cost of spiro-OMeTAD is an issue. Moreover, spiro-OMeTAD can easily provoke the degradation of perovskite structure upon thermal stress and at perceived humidity levels owing to its amorphous and highly hygroscopic nature. The following section introduces the alternative HTL materials and an outline of current

routes, which were employed to enhance the photovoltaic performance of the devices based on $MAPbI_3$ absorber.

Bi *et al*. investigated the grain growth of $MAPbI_3$ perovskite for efficient inverted-type PSCs as a function of wetting-ability of HTLs.[51] To study the effect of the wetting-ability, $MAPbI_3$ film were deposited on different wetting and non-wetting polymer substrates such as polyvinyl alcohol (PVA), poly(3,4-ethylenedioxythiophene) polystyrene sulfonate (PEDOT: PSS), crosslinked *N*4,*N*4′-bis(4-(6-((3-ethyloxetan-3-yl)methoxy)hexyl)phenyl)-*N*4,*N*4′-diphenylbiphenyl-4,4′-diamine (c-OTPD), poly(bis(4-phenyl)(2,4,6-trimethylphenyl)amine) (PTAA), and poly(*N*-9′-heptadecanyl-2,7-carbazole-alt-5,5-(4′,7′-di-2-thienyl-2′,1′,3′-benzothiadiazole)) (PCDTBT). The wetting capability of the different substrates was determined by contact angle measurement and the values of 10º, 12º, 79º, 105º and 108º were obtained for PVA, PEDOT: PSS, c-OTPD, PTAA, and PCDTBT, respectively. SEM images indicated that the average $MAPbI_3$ grain size (apparent) on c-OTPD (480 nm) is much larger than that on PEDOT: PSS (230 nm). This result indicates that a non-wetting surface can suppress the heterogeneous nucleation and facilitate grain boundary migration, resulting in low nucleation density and thus larger grain size. As a result of the reduced grain boundary area and dramatically improved crystallinity, a significant reduction in the charge recombination and charge trap density by 10–100-fold was achieved.

Pham *et al*. presented highly efficient and humidity-resistant PSCs by using two new small molecule-based HTLs, i.e, anthanthrone (ANT) dye, namely, 4,10-bis(1,2-dihydroacenaphthylen- 5-yl)-6,12-bis(octyloxy)-6,12-dihydronaphtho[7,8,1,2,3-*nopqr*]tetraphene (ACE-ANT-ACE) and 4,4′-(6,12-bis(octyloxy)-6,12-dihydronaphtho[7,8,1,2,3-*nopqr*]tetraphene- 4,10-diyl)bis(*N*,*N*-bis(4-methoxyphenyl)aniline) (TPA-ANT-TPA**)** (**Figure 3c**).[52] After extensive optimization in device processing conditions, a *PCE* of 17.5% (J_{SC} = 21.07 mA cm^{-2}, V_{OC} = 1.03 V, and *FF* = 0.80) was

achieved with negligible hysteresis for devices based on dopant-free TPA-ANT-TPA HTL whereas a slightly lower *PCE* of 13.1% with J_{SC} of 18.7 mA cm^{-2}, V_{OC} of 1.03 V, and *FF* of 0.67 was recorded for ACE-ANT-ACE based device. The doped spiro-OMeTAD HTL based device showed a *PCE* of 16.8% with J_{SC} of 21.09 mA cm^{-2}, V_{OC} of 1.04 V, and *FF* of 0.77. The difference in J_{SC} values for devices based on new HTLs was explained on the basis of the shallower HOMO level of TPA-ANT-TPA that allowed an effective hole extraction. In addition to rapid quenching of PL for TPA-ANT-TPA HTL system, a close alignment of HOMO energy levels with minimal band offset demonstrated the great potential of corresponding HTL for designing highly efficient PSCs. Because of the hydrophilic nature of the corresponding HTLs, improved stability was reported as compared to hygroscopic LiTFSI doped spiro-OMeTAD.

2.4. Interface engineering in single cation perovskites

Interface engineering is also important to further increase efficiency by improving the charge collection and by reducing the parasitic charge-carrier recombination. The effects of interface engineering on the photovoltaic performance of $MAPbI_3$ based PSCs is presented in the following section.

Wolff *et al*. carried out a systematic investigation of the energetics and the V_{OC} losses in $MAPbI_3$ PSCs with different fullerene derivatives (PCBM, C_{60}, and ICTA) employed in the ETL.[53] The analysis of energetics and the V_{OC} losses demonstrated that PCBM and C_{60} are not the ideal ETLs when targeting high V_{OC}. The fabricated devices with ICTA, which has the lowest electron affinity, i.e., the highest LUMO level among the fullerenes tested in this study, exhibited the highest V_{OC} while C_{60} with the lowest-lying LUMO level showed the lowest V_{OC} (**Figure 3d**). The insertion of an ultrathin layer of insulating polystyrene (PS) between the $MAPbI_3$ and C_{60} increased the V_{OC} by as much as 130 mV (on average 120 mV), compared to the C_{60} based control device, while maintaining the *FF* and J_{SC} values. From the

electroluminescence (EL) measurement, a better EQE_{EL} was found, indicating that non-radiative recombination of injected charge becomes progressively suppressed upon lifting the LUMO level, and it was further reduced by inserting the PS layer.

A low-temperature (140 ^oC) processed SnO_2 was employed as an ETL for $MAPbI_3$ planar PSCs on a flexible PEN (polyethylenenaphthalate) substrate.[54] A C_{60} pyrrolidine tris-acid (CPTA) was used to modify the interface between SnO_2 and $MAPbI_3$ to significantly enhance the photovoltaic performance. This flexible PSC achieved a *PCE* of 18.36% under simulated AM1.5 sunlight and maintained 75% of its initial efficiency after 500 cycles of bending with a curvature radius of 5 mm. The PL measurements of $MAPbI_3$ film on SnO_2-CPTA substrate showed a 6-fold weaker PL intensity than that of $MAPbI_3$ on pristine SnO_2, indicating the efficient extraction of electrons in the presence of CPTA.

In another interesting work, a new method of fabricating large-area flexible PSCs by inserting a conjugated polyelectrolyte interlayer (PTAA, PFNBr, and PTFTS) between the $MAPbI_3$ and HTL (graphene oxide, GO) was described (**Figure 3e)**.[55] To investigate the wettability of interlayers on GO layer, the contact angles of perovskite precursor solutions on GO/PTAA, GO/PFNBr and GO/PTFTS of 78°, 21°, and 44°, respectively, were determined, whereas the pristine GO provided a contact angle of 29°. Apparently, non-wetting surface facilities the growth of larger grains due to the dramatic suppression of heterogeneous nucleation. [51] The resulting perovskite film on GO/PTAA showed no pin-holes with an average grain size of 800 nm, whereas the average size of perovskite grains on GO/PTFTS was ~550 nm. For the best-performing GO-based device, a *PCE* of 14.91% with V_{OC} of 1.05 V, was reported while a remarkable *PCE* of 18.82% was achieved for PTFTS-modified GO HTL based devices. The GO/PTFTS (1.09 V) and GO/PTAA (1.07 V) based devices showed a higher built-in potential (V_{bi}) than pristine GO-based device (0.99 V), correlating with the V_{OC} of the corresponding devices.

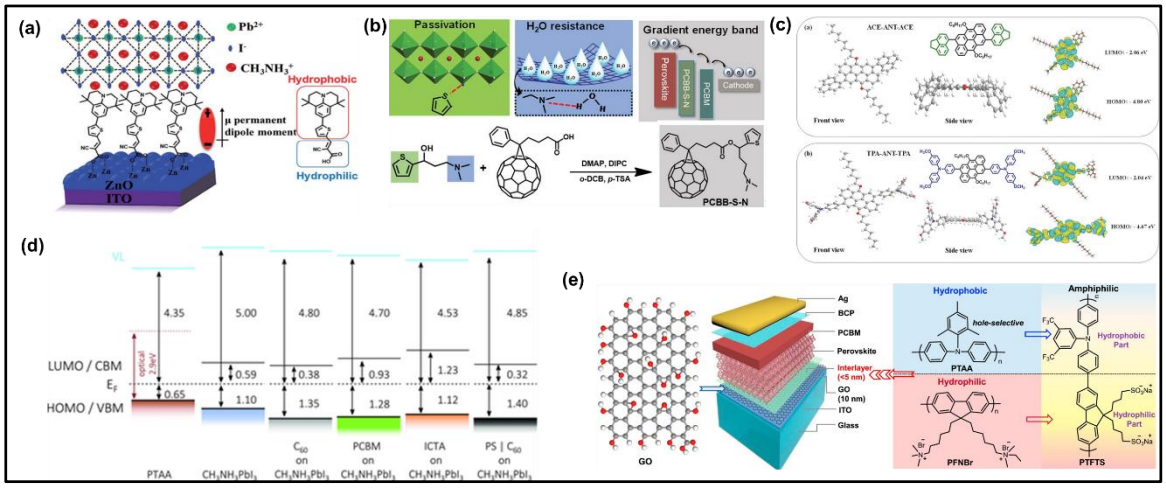

Figure 3. a) Schematic illustration of SAM-induced permanent dipole moment at the ZnO/perovskite interface. Reproduced with permission. [48] Copyright 2018, John Wiley & Sons. **b)** Design and synthesis of PCBB-S-N, with a targeted therapy effect. Reproduced with permission.[50] Copyright 2019, John Wiley & Sons. **c)** Chemical structures, geometrical configuration (front view and side view), and calculated isosurfaces and energy levels of HOMO and LUMO orbital surfaces of a) ACE-ANT-ACE and b) TPA-ANT-TPA, synthesized by classical Suzuki coupling. Reproduced with permission. [52] Copyright 2018, John Wiley & Sons. **d)** Schematic energy-level diagram of the different layers relative to E_F. Reproduced with permission. [53] Copyright 2017, John Wiley & Sons. **e)** The inverted device architecture of planar-type PSCs and the chemical structures of GO and polymer interlayers. Reproduced with permission. [55] Copyright 2019, Elsevier.

2.5. Other (Architecture) engineering in single cation perovskites

Apart from the above-mentioned engineering strategies, architecture engineering is another promising way to achieve high V_{OC}. Huang *et al*. designed a novel prismatic PSCs with light trapping configuration to mitigate the losses.[56] In the current system, incident high-to-low energy photons were separately captured by four horizontally aligned $MAPbI_xBr_{3-x}$ (x = 3, 2, 1, and 0) sub-cells with varied bandgaps. This approach generated a record V_{OC} of 5.3 V and a significant *PCE* of 21.3%, Basically, this new form of cell architecture minimized the thermodynamic losses and improved the photovoltages of PSCs by subsequently harvesting the incident photons with different energies using four different $MAPbI_xBr_{3-x}$ sub-cells. As a result of subsequent harvesting of high-to-low energy photons, the corresponding sub-cells based on $MAPbBr_3$, $MAPbIBr_2$, $MAPbI_2Br$ and $MAPbI_3$ absorber layers generated a V_{OC} of

1.54 V, 1.45 V, 1.25 V and 1.15 V, respectively, yielding a record V_{OC} of 5.3 V. This study clearly demonstrates that the mitigation of thermodynamic loss and light trapping can be achieved by carefully designing the absorption of active layers to achieve a higher V_{OC} and PCE.

Overall, the highlighted reports in this section of the review show that despite the relatively poor device stability of single-cation iodide-based PSCs, an appropriate engineering approach can dramatically improve not only photovoltaic performance but also operational stability of resulting devices. From this perspective, it is clearly evident from the above-mentioned studies that more efficient charge-transporting layers showing well-matched band alignment with perovskite can be obtained by doping and/or treatment strategies, whereas composition-additive engineering can be readily employed to form a high-quality perovskite layer with fewer trap states in the bulk and/or at the interfaces. **Table 1** summarizes the recent progress on the photovoltaic performance of single-cation iodide-based PSCs.

Table 1. V_{OC} and other photovoltaic parameters yielded by single-cation and iodide perovskite-based PSCs.

Device configuration	***Voc*** **(V)**	***Jsc*** **(mA cm^{-2})**	***FF***	***PCE*** **(%)**	**Change in *Voc* (mV)**	**Ref.**
FTO/c-TiO_2/mp-TiO_2/Perovskite + PbI_2/Spiro-OMeTAD/Au	1.09	22.42	0.79	19.09	+40	[33]
FTO/c-TiO_2/Perovskite/Spiro-OMeTAD/Au	1.15	22.82	0.68	17.80	+50	[34]
ITO/PTAA/Perovskite/Choline chloride/C_{60}/BCP/Cu	1.15	22.90	0.76	20.00	+90	[35]
ITO/PEDOT:PSS/Perovskite + H_2O/PCBM/Ca/Al	1.03	20.60	0.85	18.00	+1020	[36]
FTO/c-TiO_2/Perovskite + MASCN/Spiro-OMeTAD/Au	1.06	22.29	0.77	18.22	+430	[38]
ITO/c-TiO_2/Perovskite + IMS/Spiro-OMeTAD/Au	1.14	22.08	0.83	20.84	+40	[39]
ITO/PTAA/Perovskite + $PbCl_2$/PCBM/BCP/Ag	1.26	20.70	0.80	20.70	+15	[40]
ITO/Pedot:PSS/Perovskite + Co/PCBM/BCP/Al	1.05	21.10	0.75	17.20	+90	[44]

FTO/c-TiO_2/PCBA/Perovskite/Spiro-OMeTAD/Ag	1.16	21.38	0.72	17.76	+80	[46]
ITO/TiO_x/brookite TiO_2/Perovskite/Spiro-OMeTAD/Au	1.18	21.86	0.83	21.60	+40	[47]
ITO/JTCA-modified ZnO/Perovskite/Spiro-OMeTAD/Au	1.13	21.72	0.76	18.82	+70	[48]
ITO/Pedot:PSS/GO/Perovskite/PCBM/MoS_2/Ag	1.14	22.83	0.74	19.14	+70	[49]
ITO/PTAA/$MAPbI_3$/PCBB-S-N/PCBM/Al	1.12	23.83	0.79	21.08	+70	[50]
ITO/PTAA/Perovskite/PCBM/C_{60}/Al	1.07	22.00	0.77	18.10	+150	[51]
FTO/c-TiO_2/mp-TiO_2/Perovskite/TPA-ANT-TPA/Ag	1.03	21.05	0.80	17.50	-10	[52]
ITO/PTAA/Perovskite/PS/C_{60}/Cu	1.16	22.30	0.75	19.42	+130	[53]
ITO/CPTA-modified SnO_2/Perovskite/Spiro-OMeTAD/Au	1.08	22.39	0.75	18.36	+30	[54]
ITO/GO/PTFTS/Perovskite/PCBM/BCP/Ag	1.10	20.89	0.82	18.82	+50	[55]
FTO/c-TiO_2/mp-TiO_2/Perovskite/TPA-ANT-TPA/Ag	1.03	21.05	0.80	17.50	-10	[52]
ITO/PTAA/$MAPbI_3$ + PCBB-OEG/PCBM/Al	1.07	23.65	0.80	20.20	+30	[57]
ITO/ZnO/PVP/Perovskite/Spiro-OMeTAD/MoO_3/Ag	1.07	19.97	0.56	14.12	+70	[58]
FTO/NiO/CuI/Perovskite/PCBM/BCP/Ag	1.07	20.60	0.69	15.26	+50	[59]

3. Mixed cation and/or mixed halide-based perovskites

The functionality and performance of the perovskite absorber layer are mainly dependent on the chemical composition. Although $MAPbI_3$ perovskite material has been extensively used as a light-harnesser in device architecture, the best-performing devices use mixed cations and/or mixed halides perovskite absorber. The chemical modification of the X-site anions and A-site cations improved the optoelectronic properties and modulated the device efficiency. For instance, the introduction of formamidinium (FA^+) cations into $MAPbI_3$ structure led to the fabrication of $MA_{0.6}FA_{0.4}PbI_3$ based PSCs yielding an efficiency up to 14.9%,[60] whereas the mixed-halide perovskite composition with the substitution of 10-15 mol% of iodide with bromide facilitated a fully solution-processed PSCs with a certified efficiency of 16.2%.[61] The bandgap of mixed-halide perovskites can be effectively modulated by controlling the composition of incorporated halides, whereas the mixed-cation perovskites can make the halide redistribution thermodynamically unfavorable and consequently minimize the halide

segregation. The emerging compositions render these systems enormously appealing for designing of perovskite devices, displaying outstanding efficiency, long-term operational stability, and low process sensitivity. In the following section, we summarize the recent advances in the modification of A-site and/or X-site of the ABX_3 perovskite structure (where A is an organic ammonium cation, B is Pb^{+2} or Sn^{+2}, and X is a halide anion).

3.1. Composition-additive engineering in mixed-cation and/or mixed-halide perovskites

The overall efficiency and stability of PSCs are strongly dependent on the composition of the perovskite materials. In addition to enhanced device stability and other desirable optoelectronic properties, the mixed-halide perovskite compositions offer a great opportunity to optimize the spectral range by tuning the bandgap of the corresponding films. The incorporation of different types of halides into a crystal lattice also lead to radical changes in perovskite morphology, which can further improve the efficiency and stability of PSCs. Initially, the role of chloride remained a mystery, later studies including both electron microscopy-based analysis and bandgap studies clearly brought out that the presence of chloride can influence the growth, morphology and charge-carrier recombination without altering the bandgap of $MAPbI_3$.[62] In a similar direction, bromide was found to play a similar role, leading to significant improvement in *PCE* from 14 % to >16%.[17,18,63,64] Highly-efficient PSCs (certified *PCE* 16.2%) were initially reported for mixed-halide based $MAPb(I_{1-x}Br_x)_3$ (x=0.1–0.15) perovskite absorbing layer using solvent engineering technique.[61] A mixed solvent of γ-butyrolactone (GBL) and dimethylsulphoxide (DMSO) was used followed by a toluene drop-casting to obtain dense and fully covered perovskite films on the mesoporous TiO_2 layer. It was shown that the formation of a stable MAI(Br)–PbI_2–DMSO phase via an intercalation process during the application of a non-dissolving

solvent (toluene) was critical in retarding the rapid reaction between MAI(Br) and $PbI(Br)_2$ which enabled the formation of a highly uniform and highly crystalline perovskite films.

Recently, Longo *et al*. fabricated fully vacuum-deposited mixed-halide methylammonium lead mixed-halide $MAPb(Br_xI_{1-x})_3$ (x = 0.2 and 0.5) perovskite films with a bandgap of 1.72 and 1.87 eV.[65] The photoluminescence (PL) signal did not change under prolonged illumination at low Br^- ratio, while halide segregation was observed at high Br^- concentrations similar to solution-processed perovskite films. The absorption onset of the obtained films showed a monotonic blue-shift with increasing Br^- content. The V_{OC} increased from 1.095 V to 1.119 V to 1.207 V for devices employing perovskite with the Br^- the content of x = 0, 0.2, and 0.5, respectively (**Figure 4a**). The increase in V_{OC} of the corresponding perovskite compositions was attributed to the widening of the bandgap.

The effect of thermal treatment on the intermediate state was also investigated for hydrobromic acid (HBr) assisted fast crystallization process of mixed-halide $MAPbI_{3-x}Cl_x$ based perovskite films.[66] This approach helped to achieve rapid formation and crystallization of perovskite films after the annealing step. The enhancement in the device performance was attributed to the increased shunt resistance, lower leakage current, reduced series resistance, and stronger crystallization of the corresponding perovskite layer in the presence of HBr treatment.

In contrast to the thermally instable MA cation-based perovskites, inorganic halide perovskites such as cesium lead iodide ($CsPbI_3$) hold great promise due to their excellent thermal stability and ideal bandgap for tandem solar cell applications. However, the small size of Cs^+ cation increases the tolerance factor, and $CsPbI_3$ rapidly degrades to non-photoactive δ-phase (yellow phase) under ambient conditions. As mentioned above, the partial substitution of I^- with Br^- or sufficient treatment of $CsPbI_3$ surface helps to stabilize the α-phase of $CsPbI_3$ to make efficient PSCs. Very recently, Wang *et al*. reported a study to mitigate the

effects of cracks and pinholes in the β-$CsPbI_3$ perovskite layer by choline iodide (CHI) treatment.[67] CHI treatment increased the charge-carrier lifetime and improved the energy-level alignment between the β-$CsPbI_3$ and charge-transporting layers (**Figure 4b and 4c**). Besides improving the energy-level alignment of the conduction band minimum between β-$CsPbI_3$ and TiO_2 by 120 meV, CHI treatment fills the pinhole. The PSCs employing CHI-treated material achieved a stable efficiency reaching 18.4% (certified *PCE* of 18.3%) recorded at 45 ± 5°C under ambient conditions. As shown in **Figure 4d**, although the *Jsc* remained unaffected, the CHI-$CsPbI_3$-based PSC showed improved V_{OC} (1.05 V to 1.11 V) and *FF* (0.72 to 0.82).

Similar to $CsPbI_3$, formamidinium lead iodide ($FAPbI_3$) shows higher thermal stability than $MAPbI_3$. In addition, $FAPbI_3$ exhibits a narrower bandgap (as compared to $MAPbI_3$), however, its structural instability remains a concern particularly in the presence of moisture. Reports show that such issues of yellow-phase formation (δ-$FAPbI_3$, non-perovskite phase), halide segregation, undesired phase transition, degradation under moisture can be eliminated by using perovskites with mixed-cations compositions. For the first time, Pellet *et al.* introduced mixed-cation 3D perovskite, $(MA)_x(FA)_{1-x}PbI_3$ (x = 0–1) as an absorber layer in the mesoscopic PSCs.[60]The mixed-cation perovskite with $MA_{0.6}FA_{0.4}PbI_3$ composition showed the best photovoltaic performance, which was attributed to the enhanced harvesting and collection of red photons. The longer exciton lifetime explained the superior carrier-collection efficiency of mixed-organic-cation perovskite. Wang *et al*. reported further improvement in the device performance of ($MA_{1-x}FA_xPbI_3$) by introducing a small amount of lead thiocyanate ($Pb(SCN)_2$) additive into mixed perovskite precursor solutions.[68] The champion $MA_{0.7}FA_{0.3}PbI_3$ PSCs with 3% $Pb(SCN)_2$ additive showed *PCE* of 20.10% with a V_{OC} of 1.12 V. The increase in *PCE* was attributed to the enlarged grain size and prolonged charge carrier lifetimes revealed by time-resolved photoluminescence (TRPL) measurements.

The dependence of V_{OC} on the light intensity presented a lower slope for $Pb(SCN)_2$ incorporated perovskite-based devices, revealing a lower Shockley–Read–Hall recombination (trap-assisted recombination) in the corresponding devices.

Recently, a new method was described for fabricating gradient heterostructure of PSCs based on "intolerant" trivalent metal cations such as Sb^{3+}, and In^{3+}.[69] In this study, mixed-cation $Cs_{0.1}FA_{0.9}PbI_3$ perovskite structure was employed as the active layer due to its moderate Goldschmidt tolerant factor (τ = 0.9) and excellent photoelectrical performance.[19,70] Both the Sb^{3+} and In^{3+} do not dissolve homogeneously in the perovskite solution due to large difference in ionic sizes and electrostatic interaction between the dopants and the host Pb atoms as shown in **Figure 4e**. Therefore, a graded heterojunction was formed spontaneously. As a result, Sb^{3+} doped PSCs reached a stabilized *PCE* of 21.04% with an extraordinary *FF* and V_{OC} of 0.84 and 1.10 V, respectively. Both theoretical calculations and experimental observations specified optimized charge management as a result of the tailored band structure and interfacial electronic hybridization, promoting the charge separation and collection processes.

In order to tailor the band structure and electronic properties of perovskites, chemical modification realized by the substitution of I^- with Br^- as well as by the substitution of MA^+ with different organic/inorganic cations have been applied as an efficient approach, resulting in colour variation, high stability, and *PCE* modulation. Compositional engineering of mixed-halide and mixed-cation perovskite materials has been first reported by combining the unstable $FAPbI_3$ with $MAPbBr_3$ in $(FAPbI_3)_{1-x}(MAPbBr_3)_x$[71]. As shown in **Figure 4f**, simultaneous introduction of 15 mol% of both MA^+ cations and Br^- anions in $FAPbI_3$ led to the stabilization of $(FAPbI_3)_{0.85}(MAPbBr_3)_{0.15}$ perovskite phase. The trend in *PCE* as a function of x showed that J_{SC} increased from 19.0 mA cm^{-2} (at x = 0.05) to a maximum value of 22 mA cm^{-2} (at x = 0.15); and then decreased to 20 mA cm^{-2} (at x = 0.30), whereas V_{OC}

increased from 1.0 V to 1.12 V with increasing x. The incorporation of $MAPbBr_3$ not merely stabilized $FAPbI_3$ phase but also improved *PCE* more than 18% with negligible hysteresis.

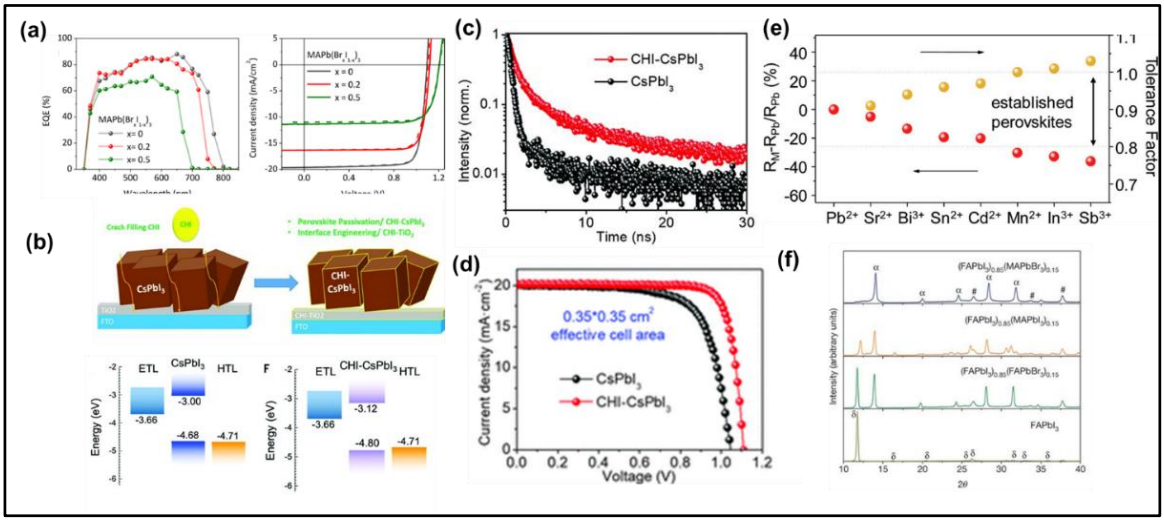

Figure 4. a) EQE spectra and *J–V* curves of the annealed devices $MAPbI_3$ (black), $MAPb(Br_{0.2}I_{0.8})_3$ (red), and $MAPb(Br_{0.5}I_{0.5})_3$ (green) (solid lines show forward scans, while dashed lines show reverse ones). Reproduced with permission.[65] Copyright 2018, American Chemical Society. **b)** Schematic illustration of crack-filling interface engineering and corresponding energy diagrams of the $CsPbI_3$ and choline iodine (CHI)-$CsPbI_3$ films, CHI treatment led to the improvement in the energy-level alignment of the conduction band minimum between β-$CsPbI_3$ and TiO_2. Reproduced with permission.[67] Copyright 2019, American Association for the Advancement of Science. **c)** TRPL decay curves of $CsPbI_3$ and CHI-$CsPbI_3$ thin films. Reproduced with permission.[67] Copyright 2019, American Association for the Advancement of Science. **d)** *J-V* characteristics of the champion PSCs based on $CsPbI_3$ and CHI-$CsPbI_3$ with 0.1-cm^2 effective cell area under simulated AM 1.5G solar illumination of 100 mW cm^{-2} in reverse scan. Reproduced with permission.[67] Copyright 2019, American Association for the Advancement of Science. **e)** $R_M - R_{Pb}/R_{Pb}$ (yellow solid circles) and tolerance factor (red solid circles) of $Cs_{0.1}FA_{0.9}MI_3$ perovskites, M = Pb^{2+}, Sr^{2+}, Bi^{3+}, Sn^{2+}, Cd^{2+}, Mn^{2+}, In^{3+}, and Sb^{3+}. Reproduced with permission.[69] Copyright 2019, John Wiley & Sons. **f)** XRD patterns of solvent-engineering-processed $FAPbI_3$, $(FAPbI_3)_{1-x}(MAPbI_3)_x$, $(FAPbI_3)_{1-x}(FAPbBr_3)_x$, and $(FAPbI_3)_{1-x}(MAPbBr_3)_x$ perovskite films (with $x = 0.15$) on mesoporous-TiO_2/blocking-TiO_2/FTO glass substrates. Reproduced with permission.[71] Copyright 2015, Nature Publishing Group.

Lead thiocyanate ($Pb(SCN)_2$) additive has also been used for the fabrication of mixed-cation mixed-halide perovskite thin films. However, the formation of excessive lead iodide (PbI_2) is still a big challenge limiting the utilization of the $Pb(SCN)_2$ additive. Yu *et al.* combined the chemical approach of additive-engineering strategy with the physical approach

of solvent annealing and reported the synergistic effects on the performance of PSCs employing wide-bandgap (bandgap of 1.75 eV) $FA_{0.8}Cs_{0.2}Pb(I_{0.7}Br_{0.3})_3$ light-absorber.[72] The authors demonstrated that the cooperation of 1.0 mol % $Pb(SCN)_2$ additive and solvent annealing can successfully facilitate the formation of large grains while avoiding the formation of excessive PbI_2. As a result, the average *PCE* increased from 13.44 ± 0.48 % to 17.68 ± 0.36 % owing to the great improvement in the V_{OC} (80 mV).

Among the various film modification approaches, polymer-assisted crystal engineering has been found to be a robust method to increase the perovskite grain size. Bi *et al*. reported the poly(methyl methacrylate) (PMMA)-templated nucleation and crystal growth of perovskite films.[73] The PMMA polymer played the dual role of enabling fast heterogeneous nucleation and slowing down the perovskite crystal growth by forming an intermediate adduct with PbI_2. As evidenced by the long PL lifetime, smooth and shiny perovskite films with excellent electronic quality were obtained. By using the $(FAI)_{0.81}(PbI_2)_{0.85}(MAPbBr_3)_{0.15}$ perovskite absorber layer, a *PCE* of 21.6% (a certified *PCE* of 21.02%) with V_{OC} of 1.14 V, *FF* of 0.78, and J_{SC} of 23.7 mA cm^{-2} was reported while the control devices showed a *PCE* of around 20% **(Figure 5a)**.

In a similar direction bis-analogue of PCBM (bis-PCBM) was utilized as a templating agent in antisolvent to obtain high electronic quality perovskite films with low-defect density.[74] It was reported that PCBM can fill the vacancies and grain boundaries on the perovskite surface and thus improve the crystallization of final perovskite film. The introduction of an electron-accepting PCBM into the $(FAI)_{0.81}(PbI_2)_{0.85}(MABr)_{0.15}(PbBr_2)_{0.15}$ film facilitated the slow electron extraction resulting in a *PCE* of 20.8%. The increase in J_{SC} with PCBM was ascribed to the enhanced photoelectron transport, higher conductivity, and higher mobility whereas the origin of the improved V_{OC} was the reduction of spontaneous trap-assisted non-radiative recombination.

Although MA-FA based perovskite materials dramatically improved the photovoltaic performance of PSCs, these compositions are sensitive to the processing conditions because of their intrinsic structural and thermal instability issues. To overcome these issues, composition-additive engineering involving the mixing of MA/FA organic cations with small amounts of inorganic cations has been intensively investigated in recent years. High-quality perovskite films were obtained by incorporating a small amount of inorganic cesium (Cs) cation into the MA/FA composition. The obtained triple-cation $Cs_{0.05}(MA_{0.17}FA_{0.83})_{0.95}Pb(I_{0.83}Br_{0.17})_3$ perovskite absorber yielded a stabilized *PCE* exceeding 21% with a V_{OC} of 1.13 V and excellent operational stability (**Figure 5b**).[21] In another study, small and oxidation-stable rubidium cations (Rb^+) were explored to further improve the properties of perovskite material and the photovoltaic efficiency of resulting PSCs.[22] Stabilized *PCE* of 21.6% with a V_{OC} of 1.19 V was obtained from PSCs based on RbCsMAFA perovskite composition containing 5% Rb additive. The best device showed an outstanding V_{OC} of 1.24 V with a loss in the potential of only ~0.39 V, implying negligible nonradiative recombination losses. The obtained electroluminescence of 3.8% further confirmed a strong suppression of nonradiative recombination in the RbCsMAFA device. The electrochemical characterization also brought out that the introduction of Rb^+ improves the interfacial charge transport characteristics in multiple-cation mixed-halide PSCs.[75,76]

Recently, in order to further boost the photovoltage of mixed-cation and mixed-halide based PSCs, guanidinium iodide (GuaI) was introduced into $Cs_{0.05}(MA_{0.17}FA_{0.83})_{0.95}Pb(I_{0.83}Br_{0.17})_3$ perovskite films.[77] GuaI led to the suppression of parasitic charge-carrier recombination and enabled fabrication of efficient PSCs (>20% *PCE*) yielding reproducible V_{OC} as high as 1.20 V (**Figure 5c**). The 70 mV enhancement in V_{OC} was ascribed to the reduced non-radiative recombination as revealed by time-resolved photoluminescence and electroluminescence measurements (**Figure 5d**).

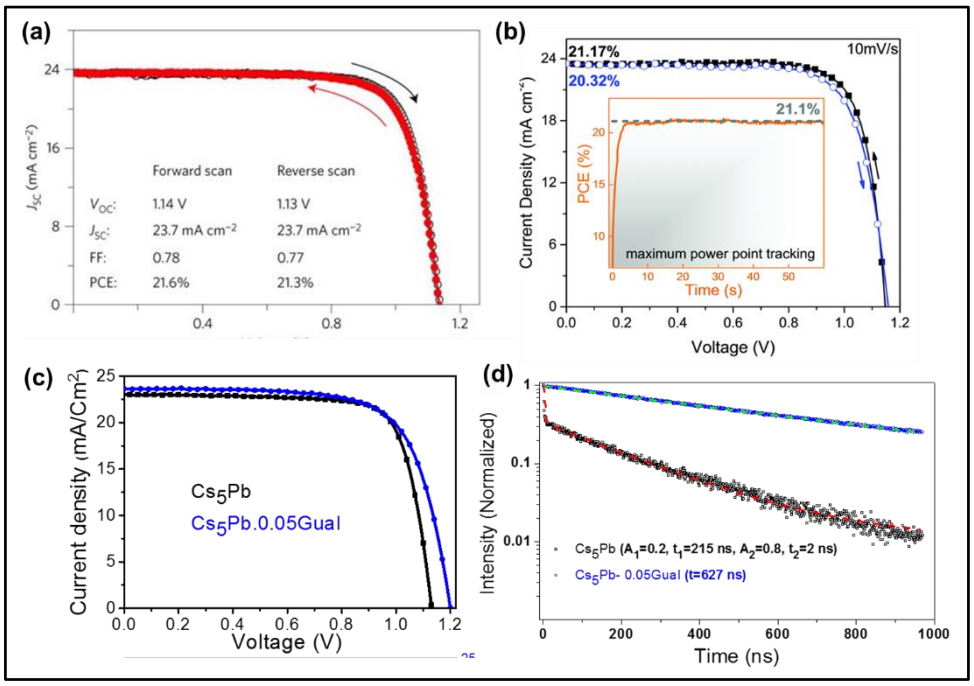

Figure 5. a) *J-V* curves of the champion PSC prepared by polymer-templated nucleation and growth method displaying the best *PCE* of 21.6% with a PMMA concentration C_{PMMA} = 0.6 mg ml^{-1}. Reproduced with permission.[73] Copyright 2016, Nature Publishing Group. **b)** *J-V* and stability characteristics (for the best performing Cs_5M device. The inset shows the power output under maximum power point tracking for 60 s. Reproduced with permission.[21] Copyright 2016, Royal Society of Chemistry. **c)** *J-V* curves of the best devices based on Cs_5Pb and $Cs_5Pb_{0.05}GuaI$ perovskite films, 5% GuaI to Cs_5Pb significantly improved the V_{OC} from 1.13 V to 1.20 V. Reproduced under the terms of the CC BY 4.0 license.[77] Copyright 2019, Science and Technology Review Publishing House **(d)** TRPL spectra of pure and GuaI containing perovskite films, charge carrier lifetime values of 215 ns and 627 ns were estimated, respectively, for the Cs_5Pb, and $Cs_5Pb_{0.05}GuaI$ perovskite films. Reproduced under the terms of the CC BY 4.0 license.[77] Copyright 2019, Science and Technology Review Publishing House.

The suppression of defects resulting in an increase in the V_{OC} has also been reported for halide-based additives. For example, Fu *et al*. introduced an additive-engineering strategy by adding formamidine acetate (FAAc) to the perovskite-precursor solution.[78] The role of FAAc was explained on the basis of chemical reactions between FAAc and methylammonium iodide (MAI) which forms formamidinium iodide (FAI) and methylammonium acetate (MAAc). In this way, the number of I^- vacancies could be reduced at the surface due to lower thermal stability of MAAc instead of MAI, leading to a reduced recombination rate in the resulting perovskite films. TRPL and thermogravimetric analysis **(**TGA) results confirmed the

stabilization of I^- anions by Ac^- anions. By using such an additive in $Cs_{0.05}FA_{0.81}MA_{0.14}Pb(I_{2.55}Br_{0.45})$ based perovskite film, the V_{OC} of 1.19 V was achieved with the best *PCE* of 21.9%.

3.2. ETL engineering in mixed cation and/or mixed halide perovskites

One of the most important layers in obtaining the high V_{OC} is the ETL, which facilitates the extraction and transport of electron as discussed in section 2.2. Therefore, a suitable energy level alignment and a trap-free surface are critical to achieving admissible *PCE*. ETL engineering is one of the most efficient ways to acquire a high-quality electron conductor with well-matched energy level and low trap-states and/or pin-holes. In this section, the remedial ETL engineering strategies employed for mixed-cation and/or mixed-halide based perovskite devices are discussed.

Zhou *et al*. reported the doping of TiO_2 ETL with yttrium (Y^{3+}) ions and modification of ITO substrate with poly-ethyleneimine ethoxylated (PEIE) to suppress the carrier recombination in the perovskite film and to facilitate the carrier injection into the carrier transport layers[79]. By PEIE modification, the work function of ITO was reduced from -4.6 eV to -4.0 eV, whereas Y^{3+} doping increased the conduction band minimum (CBM) up to -4.0 eV. As a result of these modifications, a *PCE* (only reverse scan) of 19.3% with V_{OC} of 1.15 V, was achieved for n-i-p-type PSCs in a planar configuration. The 110 mV increase in V_{OC} was mainly attributed to the reduced non-ideal space charge distribution as a result of balanced carrier transport. Notably, the *PCE* measured by a reverse scan can be highly overestimated owing to the large-hysteresis index. The anomalous hysteresis in PSCs can mainly be explained by the evoking the charge migration or accumulation at the perovskite/ETL interface. The enhancement in electrical properties and reduction in surface defects of ETL by suitable dopants can reduce the non-radiative recombination at the

perovskite/ETL interface and thereby properly alleviate the anomalous hysteresis behaviour of PSCs.

In an interesting study, a new mesoscopic architecture using Cs-doped TiO_2 beads as electron selective contact was described.[80] The enhancement of the contact area accessed by the perovskite light absorber and interface passivation between perovskite and mp-TiO_2 led to the fabrication of efficient quadruple-cation (Rb/Cs/$FA_{0.95}MA_{0.05}$) perovskite-based PSCs with negligible hysteresis (**Figure 6a**). This substantially reduced hysteresis as compared to the bare TiO_2, which was attributed to less charge accumulation at the perovskite/Cs-doped TiO_2 interface. It was also demonstrated that Cs doping induces a shift of both oxygens (O) 1s and titanium (Ti) 2p peaks to lower energy, thereby decreasing oxygen vacancy which functions as an electron trap. This study obviously showed that a reduction in recombination rate is directly related to the increase in V_{OC} of devices. Another electron selective contact that has gained considerable attention for enhancement of photovoltage is SnO_2, which has a deeper conduction band and a suitable band alignment with the perovskite absorber. A low-temperature atomic layer deposition (ALD) method was reported to fabricate compact and pin-hole free SnO_2 ETL for their application in planar PSCs exhibiting a high performance (> 18%) with high voltages up to 1.19 V.[81] The low hysteresis is a result of suitable band alignment and good charge collection for SnO_2 based devices, whereas, amorphous TiO_2 based devices showed a strong hysteresis and a low J_{SC} (**Figure 6b**). The UPS and femtosecond TA measurements indicated a barrier-free charge transport across the perovskite/SnO_2 in contrast to the perovskite/TiO_2 interface. Recently, the suppression of hysteresis in planar-type PSCs was also reported using EDTA-complexed SnO_2 ETL with a striking *PCE*.[82] EDTA-complexed SnO_2 provided a well-matched Fermi level with the conduction band of mixed-cation $FA_{0.95}Cs_{0.05}PbI_3$ perovskite structure, leading to a higher V_{OC}. In addition, the electron mobility EDTA-complexed SnO_2 ETL was found to be three

times higher than that of the pristine SnO_2. The record *PCE* of corresponding PSCs based on EDTA-complexed SnO_2 ETL was achieved to be 21.60% (certified as 21.52% by Newport) while pristine SnO_2 ETL based device showed only a *PCE* of 18.93%. As shown in (**Figure 6c**), the hysteresis in the EDTA-complexed SnO_2 ETL based device drastically reduced because of the eliminated charge accumulation between perovskite and ETL interface. It was also reported that EDTA treatment made the SnO_2 surface more hydrophilic, thus, decreasing the Gibbs free energy for heterogeneous nucleation, resulting in high-quality perovskite films.

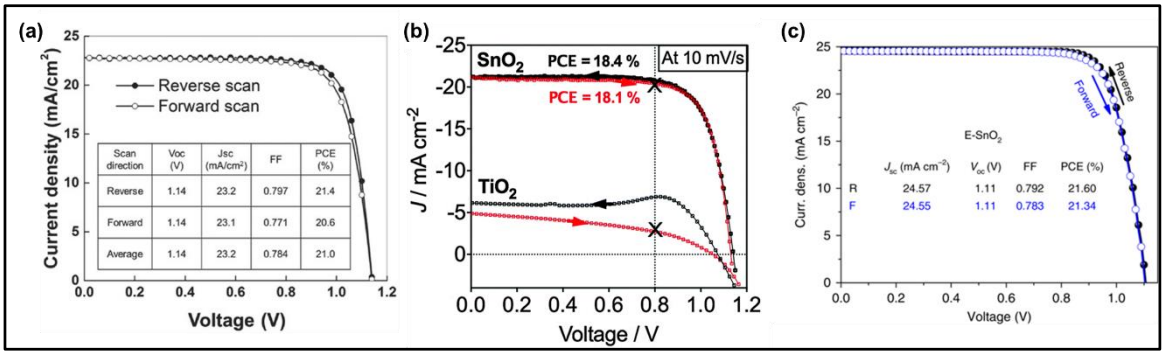

Figure 6. a) *J-V* curves of the top-performing devices prepared with CsBr-doped mp-TiO_2 as ETL. Reproduced with permission.[80] Copyright 2018, John Wiley & Sons. **b)** *J-V* properties of TiO_2 and SnO_2-based planar $(FAPbI_3)_{0.85}(MAPbBr_3)_{0.15}$ devices backward scan (black curve) and reversed scan (red curve). Reproduced under the terms of the CC BY-NC 3.0 license.[81] Copyright 2015, Royal Society of Chemistry. **c)** *J-V* curves of the device using EDTA-complexed SnO_2 E-SnO_2 as ETL in forward and reverse direction. Reproduced under the terms of the CC BY-NC 4.0 license.[82] Copyright 2018, Nature Publishing Group.

Gong *et al*. systematically investigated the band offset between ETL and $(FAPbI_3)_{0.85}(MAPbBr_3)_{0.15}$ perovskite absorber by tuning F-doping level in gradient SnO_2 based ETL.[83] A reduction in the band offset was reported by the gradual substitution of F^- anions, resulting in a reduction in energy loss and a dramatic increase in V_{OC}. By employing the bilayer ETLs, planar type PSCs reached to a *PCE* of 20.2% with a V_{OC} of 1.13 V, while the control device showed a *PCE* of 16.3% with a V_{OC} of 1.03 V. Compared to pristine SnO_2 ETL, the bilayer ETL showed a lower surface roughness, higher electrical conductivity, and

upward-shifted Fermi level. More importantly, in addition to longer lifetime constant of bilayer ETL/perovskite (~356.5 ns) than that of pristine SnO_2 ETL/perovskite (~198.7 ns); bilayer ETL exhibited better carrier collection and effectively suppressed the carrier recombination.

In a similar direction, a thin layer of LiF at the SnO_2/perovskite interlayer was introduced to fabricate high efficiency PSCs.[84] It was deduced that the LiF interlayer acts as a highly efficient interfacial passivation layer between SnO_2/perovskite interface without influencing the surface topography and crystal quality of perovskite films as well as light absorption ability of devices. In the presence of 1 nm thick LiF layer, the V_{OC} increased from 1.06 V to 1.16 V, indicating that LiF suppressed the interfacial trap states between SnO_2/perovskite and reduced the interfacial (parasitic) charge recombination. The role of Li^+ and F^- was also investigated separately, by using the interlayer of PbF_2 (F^- only) and LiTFSI (Li^+ only) layers. It was found that a thin PbF_2 modified SnO_2 layer increased the V_{OC} from 1.06 V to 1.14 V, while LiTFSI did not change it. Therefore, the effect of F^- ions was the key factor in V_{OC} improvement.

In addition to doping based modifications, the preparation of the ETL is also important to obtain efficient devices. A low-temperature solution-processed chemical bath deposition (CBD) method was described for Nb-doped SnO_2 layers for almost hysteresis-free and highly efficient $(FAPbI_3)_{0.85}(MAPbBr_3)_{0.15}$ perovskite-based planar type PSCs.[85] ETLs with an optimum Nb-doping (5 mol.%) exhibited a lower series resistance, resulting in a higher *FF* (0.74 in average) and suppressed *J-V* hysteresis. This approach generated a V_{OC} of 1.16 V and a significant *PCE* of 20.47% for the device employing 5 mol.% Nb-doped ETL. Such an improvement in V_{OC} was attributed to the reduced recombination at the interface due to the formation of defect-free and high-quality surface coverage.

3.3. HTL engineering in mixed-cation and/or mixed-halide perovskites

As described in Section 2.3. HTLs play a key role in extracting and transporting the photo-generated holes and in achieving an admissible photovoltaic performance. In addition to reasonable hole mobility and high electrical conductivity, HTL should meet requirements such as well-aligned energy levels, low-cost synthesis, and excellent thermal/photochemical stability.[86,87] Towards this end, different strategies in HTL engineering, i.e. additives, molecular engineering, new materials, have been investigated. In the following section, some of the most representative reports regarding photovoltaic performance and stability of mixed-cation mixed-halide PSCs will be discussed.

In spiro-OMeTAD based systems, the dopants play a key role in recombination dynamics to limit the V_{OC} because they act as recombination centres at the HTL interface. The effect of dopant concentration of spiro-OMeTAD was examined on the recombination dynamics and it was found that the recombination is strongly dominated by the dopants and a V_{OC} can significantly boost up to 1.23 V by reducing the Li-TFSI concentrations in spiro-OMeTAD (**Figure 7a**).[88] However, lower dopant concentrations also yielded a lower *FF*, resulting in a decrease in the overall *PCE*, showing that the dopant is indispensable in the case of spiro-OMeTAD owing to its low conductivity and hole mobility.

Other dopants have been also explored to enhance photovoltaic performance. Among the various alternates, Zn-$TFSI_2$ was successfully employed in spiro-OMeTAD as a *p*-type dopant by Seo *et al*., leading to improved hole mobility (from 3.78 x 10^{-3} cm^2 V^{-1} s^{-1} to 3.83 x 10^{-2} cm^2 V^{-1} s^{-1}) and hole separation compared to the Li-TFSI.[89] The device with Zn-$TFSI_2$ exhibited an 80 mV higher built-in voltage and a larger recombination resistance as compared to those based on Li-TFSI, leading to the striking increase in both the V_{OC} and *FF*. Zn-$TFSI_2$ employing devices showed a stabilized *PCE* of 22% with a V_{OC} of 1.15 V owing to the downward shifting of the Fermi level of spiro-OMeTAD (**Figure 7b**). Furthermore, Zn-$TFSI_2$

employing devices presented an excellent photo-stability, showing even a 2% increase after 600 h light soaking. The remarkable photovoltaic performance was ascribed to the electronic properties of the Zn-$TFSI_2$, whereas outstanding long-term stability was attributed to the static nature and higher electric-field strength of the Zn ions, inducing a strong electrostatic interaction within the spiro-OMeTAD matrix.

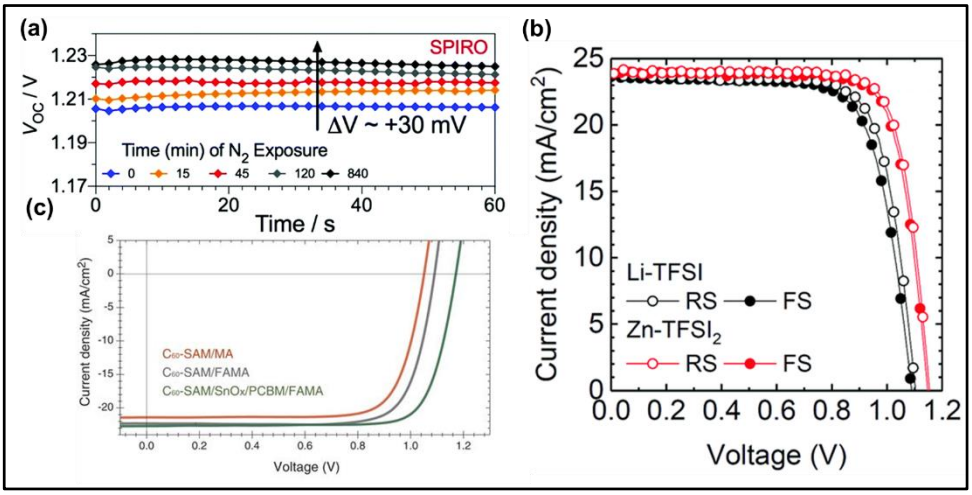

Figure 7. a) V_{OC} *vs.* time with nitrogen exposure for best-performing devices using spiro-OMeTAD as HTL. Reproduced with permission.[88] Copyright 2017, Royal Society of Chemistry. **b)** *J-V* curves of devices employing Li-TFSI or Zn-$TFSI_2$ as a dopant for spiro-OMeTAD. Reproduced with permission.[89] Copyright 2018, Royal Society of Chemistry. **c)** *J-V* curves of the maximized performance devices for MA perovskite using C_{60}-SAM as ETL (orange curve) and PDCBT/Ta-WO_x as HTL, FAMA perovskite-based devices using C_{60}-SAM as ETL and PDCBT/Ta-WO_x as HTL (gray curve), and FAMA perovskite-based devices using C_{60}-SAM/SnO_x/$PC_{60}BM$ as ETL and PDCBT/Ta-WO_x as HTL (green curve). Reproduced with permission.[91] Copyright 2017, American Association for the Advancement of Science.

In addition to TFSI based dopants, different additives have been also explored to reduce the non-radiative recombination losses. The synthesis and utilization of adamantylammonium halides (ADAHX, X = Cl^-, Br^-, I^-) as a promising dopant in spiro-OMeTAD was recently reported.[90] Solid-state NMR spectroscopy showed a strong interaction between ADAHI and perovskite surface, resulting in highly efficient PSCs (22%). The insertion of ADAHI dopant into spiro-OMeTAD increased the V_{OC} by 145 mV (from 1.10 V to 1.245 V). The loss in the potential for the corresponding devices was reported to be

only 365 mV with respect to the bandgap of 1.61 eV. The recombination behaviour at perovskite and HTL interface was investigated by electron beam-induced current (EBIC), which demonstrated a strong and uniform signal in the presence of ADAHI, indicating a lower recombination rate owing to the successful suppression of interfacial traps.

In addition to interfacial traps, the energy barriers between the HTL interfaces play a key role in minimizing the charge-carrier transport losses in PSCs. Bilayered HTLs are one of the best ways to decrease the energy barriers, which not only show a good selectivity but also a low-resistivity. Hou *et al*. reported tantalum-doped tungsten oxide (Ta-WO_x) and a polythiophene derivative, poly[5,5′-bis(2-butyloctyl)-(2,2′-bithiophene)-4,4′-dicarboxylate-alt-5,5′-2,2′-bithiophene] (PDCBT) conjugated polymer multilayers to reduce interfacial barrier and form quasi-ohmic contacts.[91] By employing the perovskite composition of $FA_{0.83}MA_{0.17}Pb_{1.1}Br_{0.50}I_{2.80}$ and ionic dopant–free HTL, a *PCE* of 21.2% with negligible hysteresis was achieved (**Figure 7c**). A thin coating of high conductive Ta-WO_x film onto PDCBT showed a shift of 0.5 eV in work function, implying much more effective charge transfer from the polymer to the metal oxides.

The concept of molecular engineering of the perovskite layer and HTL is crucial to increase the V_{OC} and improve the performance of PSCs. In general, a higher *Voc* is obtained for HTMs with a higher oxidation potential. However, factors like intrinsic mobility of the HTM material, optimization of HTM molecular structure are equally important to enhance $V_{OC.}$ The introduction of an electron-withdrawing group such as fluorine with a high electronegativity to organic conjugated materials has been demonstrated as an efficient route to alleviate the charge transfer by controlling the energetic offset and improve the V_{OC} values of polymer-based PSCs. For example, Kim *et al*. investigated the impact of fluorination on poly(triarylamine) (PTAA) polymers hole-transporting materials in $(FAPbI_3)_{0.85}(MAPbBr_3)_{0.15}$ based mesoporous n-i-p structure PSCs.[92] The fluorination

successfully led to downshifting of the highest occupied molecular orbital (HOMO) level of PTAA derivatives (−5.14 eV to −5.63 eV), leading to an increase in the V_{OC} (1.10 V to 1.14 V) (**Figure 8a and 8b**). Space-charge-limited current (SCLC) measurements revealed hole mobility in the order of 10^{-5} while TRPL measurement showed a better charge extraction from perovskite compared with the reference PTAA HTL.

In a similar direction, fluorene-terminated HTL material ((N2,N2′,N7,N7′-tetrakis(9,9-dimethyl-9H-fluoren-2-yl)-N2,N2′,N7,N7′-tetrakis(4-methoxyphenyl)-,9′-spirobi[fluorene]-2,2′,7,7′-tetraamine)) (abbreviated as DM) with a high glass transition temperature was synthesized for efficient $(FAPbI_3)_{0.95}(MAPbBr_3)_{0.05}$ based PSCs. By using obtained material, *PCE* of 22.9% with certified efficiencies of 22.6% for small-area (~0.094 cm^2) devices and 20.9% for large-area (~1 cm^2) was demonstrated (**Figure 8c**).[93] The obtained V_{OC} of 1.14 V was ascribed to the slightly higher oxidation potential of DM HTL, leading to better energy-level matching with the perovskite as shown in (**Figure 8d**). HTL engineering strategies have also been applied for inverted device architecture in order to further improve the photovoltaic performance stability. In the inverted structure of PSCs, nickel oxide (NiO) is one of the most efficient HTL material owing to its wide bandgap, high hole mobility, and appropriate valence band edge.[94,95] Bai *et al*. demonstrated that surface modification of NiO HTL in inverted type PSC with di-ethanolamine (DEA) molecules can enhance the hole extraction/transport and thus the photovoltaic performance.[96] The enhancement in photovoltaic performance was ascribed to the favourable layer formed by the molecular adsorption and the better interfacial interaction. The molecular adsorption creates a dipole layer, which is favourably oriented for hole extraction resulting in higher device performance (*FF*: 0.80 and *PCE*: 15.9%) for DEA based PSC than the control device (*FF*: 0.65 and *PCE*: 11.2%).

Recently, molecular doping was introduced to modify the solution-derived NiO_x HTLs by simply spin-coating an acetonitrile solution of 2,2′-(perfluoronaphthalene-2,6-

diylidene)dimalononitrile (F6TCNNQ) onto the bare NiO_x.[97] This approach helped the molecular dopants to penetrate into the grain boundaries of the bare NiO_x film, which resulted in a strong *p*-type doping effect, thus leading to a remarkable reduction in contact resistance at the NiO_x–perovskite interface. Moreover, the Fermi level of NiO_x was increased from 4.63 eV to 5.07 eV after the F6TCNNQ doping, while the valence band maximum (VBM) level was decreased from 5.21 eV to 5.37 eV, leading to an increase in V_{OC} and overall PCE in inverted CsFAMAPb$(IBr)_3$-based devices, owing to the minimized thermionic losses (**Figure 8e and f**).

Very recently, low temperature and solution-combustion based method was employed to prepare the NiO_x HTL.[98] The resulting NiO_x exhibited a high film quality, slightly larger bandgap and preferable energy alignment with respect to $MA_{1-y}FA_yPbI_{3-x}Cl_x$ perovskite layer compared to high-temperature sol-gel-processed NiO_x. The devices employing combustion-derived NiO_x showed that the perovskite films on corresponding HTL had larger grain size with fewer defect states, exhibiting a high *PCE* of 20.2% with a remarkable V_{OC} of 1.12 V. The improved *PCE* and enhanced ambient air storage stability was ascribed to the high quality of perovskite/HTL interface resulting in an enhanced charge transport, extraction, and suppressed charge recombination whereas the enhancement in V_{OC} was attributed to the decreased work function which increases the potential difference between valance band of NiO_x and conduction band of perovskite.

In addition to inorganic NiO HTL, organic-based poly(3,4-ethylenedioxythiophene): poly(styrene sulfonate) (PEDOT: PSS) is widely used as an HTL material in perovskite devices owing to its low-temperature processability, suitable valance band maximum, and low surface roughness. However, the high acidic nature and large energy barrier between the perovskite/PEDOT: PSS layers limit the hole extraction. To improve the hole extraction properties of PEDOT: PSS HTL, several attempts have been reported. For example, graphene

oxide (GO) was doped into PEDOT: PSS HTL and excellent optical and electrical properties including high electrical conductivity, high Fermi level, and high quality of perovskite crystal were reported (**Figure 8g**).[99] The device employing GO doped PEDOT: PSS facilitated an efficient hole extraction and higher V_{OC} (1.02 V) as compared to a control device (0.97 V). As a result, a *PCE* of 18.09% has been obtained with negligible hysteresis.

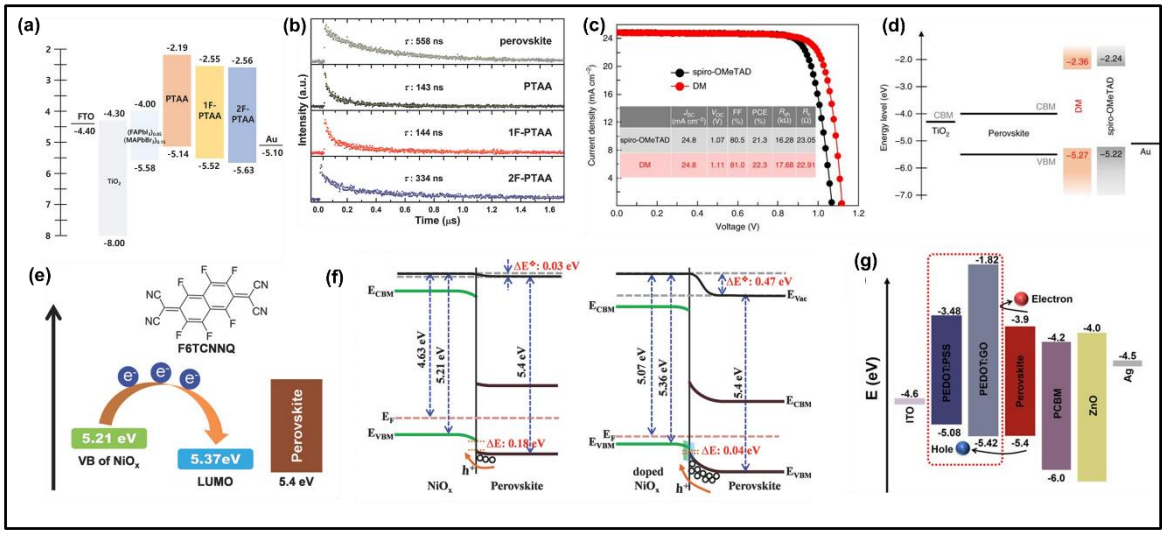

Figure 8. a) Schematic illustration of energy level alignment of perovskite devices with PTAA derivatives as HTLs. Reproduced with permission.[92] Copyright 2018, John Wiley & Sons. **b)** TRPL decay curves of pristine perovskite, PTAA, 1F-PTAA, and 2F-PTAA deposited on perovskites. Reproduced with permission.[92] Copyright 2018, Wiley. **c)** *J-V* curves of the average measured efficiency for the perovskite devices using spiro-OMeTAD and DM as HTL, the device using DM showed a higher V_{OC}. Reproduced with permission.[93] Copyright 2018, Nature Publishing Group. **d)** Energy level diagram of DM and spiro-OMeTAD. Reproduced with permission.[93] Copyright 2018, Nature Publishing Group. **e)** Chemical structure of molecular dopant F6TCNNQ and energy band alignment of NiO_x and molecular dopants of F6TCNNQ and the chemical structure. Reproduced with permission.[97] Copyright 2018, Wiley. **f)** Impact of molecular doping of F6TCNNQ on the band bending at p-type doped NiO_x–perovskite interface. Reproduced with permission.[97] Copyright 2018, Wiley. **g)** The relative energy levels of the various device components in the ITO/HTL/perovskite/PCBM/ZnO nanoparticles/Ag perovskite device. Reproduced under the terms of the CC BY-NC 4.0 license.[99] Copyright 2018, Nature Publishing Group.

3.4. Interface engineering in mixed cation and/or mixed halide perovskites

In addition to trap-assisted recombination in the perovskite layer, minority carrier recombination at the perovskite/charge transport layer interfaces is another crucial obstacle in

PSCs. Stolterfoht *et al*. investigated non-radiative recombination pathways in planar inverted-type PSCs with undoped organic charge transport layers.[100] The conjugated polyelectrolyte poly[(9,9-bis(30-((N,N-dimethyl)-N-ethylammonium)-propyl)-2,7-fluorene)-alt-2,7-(9,9-dioctylfluorene)] dibromide (PFN-P2) and LiF were used as interfacial layers to suppress the recombination losses. Inserting ultrathin interlayers (<1 nm) between the perovskite absorber and charge transport layers (PTAA/perovskite and perovskite/C_{60}) led to a substantial reduction in the interfacial recombination losses by 65 meV and 35 meV for *p*- and *n*-contacts, respectively. This approach enabled a dopant-free 1 cm^2 PSCs with an efficiency exceeding 20% (19.83% certified *PCE*) with a remarkable V_{OC} (1.17 V) and *FF* (>0.81) (**Figure 9a**). High-quality $CsPbI_{0.05}[(FAPbI_3)_{0.89}(MAPbBr_3)_{0.11}]_{0.9}$ perovskite film exhibited a lifetime around 500 ns while perovskite/transport layer heterojunctions showed fast decay potentially allowing a high V_{OC} (**Figure 9b**). A similar approach was introduced by Peng *et al*. applying a double-side polymer poly(methyl methacrylate) (PMMA) at TiO_2/perovskite and perovskite/spiro-OMeTAD interfaces.[101] The remarkable passivation properties of PMMA increased the V_{OC} from 1.10 ± 0.01 V for the control device to 1.16 ± 0.01 V for perovskite/ETL interface- passivation, and 1.20 ± 0.01 V for double-side passivated devices. As a result, a high *PCE* of 20.8% was achieved with a significant V_{OC} of 1.22 V while using ~1.6 eV bandgap $Cs_{0.07}Rb_{0.03}FA_{0.765}MA_{0.135}PbI_{2.55}Br_{0.45}$ layer (**Figure 9c**). Photoluminescence imaging and transient spectroscopic measurements showed a lower non-radiative recombination rate (**Figure 9d**) whereas surface analysis indicated a good filling of pinholes, and unspecified passivation of surface traps/defects, yielding an improved V_{OC} without any significant degradation in J_{SC} or *FF*. The analysis of perovskite-PMMA molecular interactions reveals that the Lewis-base nature of the oxygen atoms in the carbonyl (C=O) groups (donor electrons) on the PMMA can aid in the reduction of Pb^{2+}defect ions at the perovskite/ETL and perovskite/HTL interfaces.

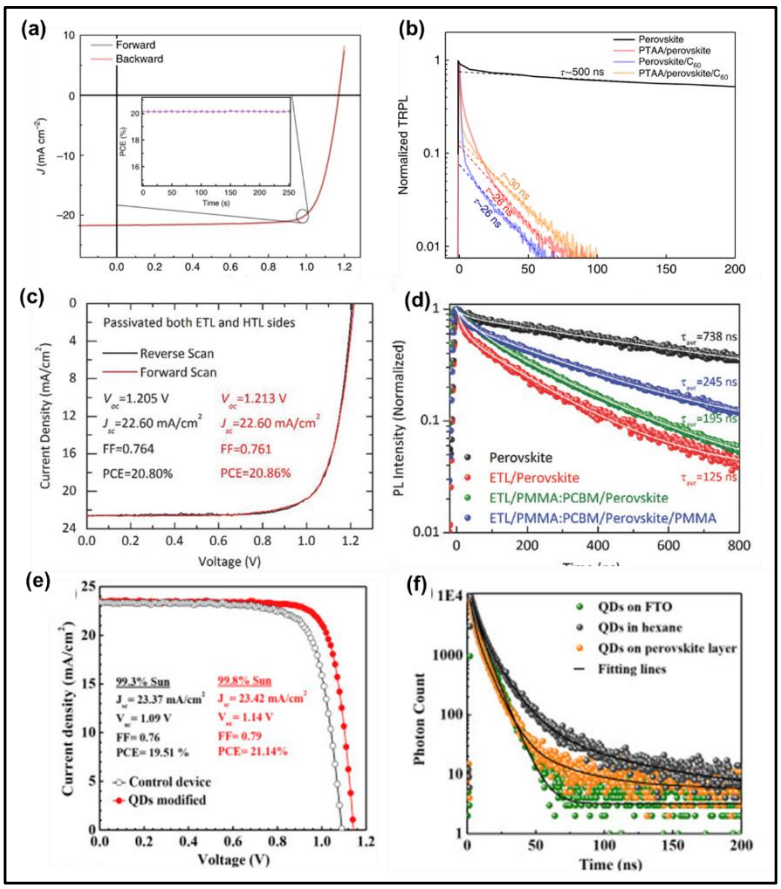

Figure 9. a) *J-V* curves of the 1 cm^2 perovskite cells reaching 20% PCE using a combination of PFN-P2 and LiF interlayers. Reproduced with permission.[100] Copyright 2018, Nature Publishing Group. **b)** TRPL decay of a pristine perovskite film showing mono-exponential lifetime (~500 ns) and bi-exponential decay for perovskite/charge transport layer heterojunctions. Reproduced with permission.[100] Copyright 2018, Nature Publishing Group. **c)** *J-V* curves of the double-side passivated device with an architecture of FTO/c-In-TiO_x/m TiO_2/PMMA: PCBM/Perovskite/PMMA/Spiro-OMeTAD/Au. Reproduced with permission.[101] Copyright 2018, Wiley. **d)** TRPL measurements of ETL only samples (illuminated from the ETL side): perovskite, ETL/perovskite, ETL/PMMA: PCBM/Perovskite and ETL/PMMA: PCBM/Perovskite/PMMA. Reproduced with permission.[101] Copyright 2018, Wiley. **e)** *J-V* curves for the champion cells for bare and QDs-10 modified perovskite-based devices. Reproduced with permission.[102] Copyright 2019, Elsevier. **f)** TRPL decays of the bare and QDs-10 modified perovskite films with and without spiro-OMeTAD layer. Reproduced with permission.[102] Copyright 2019, Elsevier.

In addition to organic passivation materials including fullerene derivatives or PMMA, more recently Akin *et al*. developed a promising approach to modify the perovskite/HTL interface employing inorganic $CsPbBr_{1.85}I_{1.15}$ perovskite quantum dots (PQDs) as an interfacial layer.[102] By the insertion of the interfacial layer, *PCE* of the best-performing

device increased from 19.51% to 21.14% with a remarkable increase in *FF* and V_{OC} (**Figure 9e**). The increase in *FF* (0.76 to 0.79) was attributed to enhanced hole extraction and suppressed carrier recombination at the interfaces and grain boundaries whereas such an increase in V_{OC} (1.09 V to 1.14 V) was ascribed to the photo-induced dipole effect originating from the accumulated charges on the perovskite surface and suitable energy level of PQDs layer. The dipole effect positively shifted the perovskite energy bands whereas PQDs layer hindered the back-flow of electrons towards the HTL, minimizing parasitic charge-carrier recombination (**Figure 8f**). **Table 2** summarizes the recent progress on the photovoltaic performance of mixed cation and/or mixed halide-based perovskite devices. In this section, we have covered the strategies including; 1) solvent/polymer-assisted crystal engineering for fast crystallization resulting in perovskite films of high electronic quality, 2) compositional engineering for example by addition of inorganic cations for perovskite films with low defect density, 3) band alignment engineering using modified charge transport layers such as doped SnO_2, modified state-of-the-art HTL spiro-OMeTAD, molecular engineering of perovskite and HTLs, and 4) use of interfacial layers to suppress recombination losses. These studies clearly indicate that the development of strategies to improve performance and stability of mixed cation and/or mixed halide-based PSCs is an important application-driven research topic.

Table 2. V_{OC} and other photovoltaic parameters of mixed cation and/or mixed halide perovskite-based PSCs.

Perovskite composition	**Device configuration**	***Voc*** **(V)**	***Jsc*** **(mA cm^{-2})**	***FF***	***PCE*** **(%)**	**Change in *Voc* (mV)**	**Ref.**
$CsFAMAPb(I,Br)_3$	FTO/c-TiO_2/mp-TiO_2/Perovskite/Spiro-OMeTAD/Au	1.13	22.69	0.75	21.10	+10	[21]
$RbCsFAMAPb(I,Br)_3$	FTO/c-TiO_2/mp-TiO_2/Perovskite/Spiro-OMeTAD/Au	1.19	22.80	0.81	21.80	+50	[22]

$MAPb(Br,I)_3$	ITO/C_{60}-PhIm/Perovskite/TaTm/Au	1.21	10.50	0.79	10.00	+110	[65]
$MAPb(Cl,I)_3$	ITO/c-TiO_2/Perovskite:HBr/Spiro-OMeTAD/Ag	0.94	21.71	0.77	15.76	+50	[66]
$FAMAPbI_3$	FTO/SnO_2/C_{60}-SAM/Perovskite + $Pb(SCN)_2$/Spiro-OMeTAD/Au	1.11	22.34	0.81	20.03	+10	[68]
$CsFAPbI_3$	FTO/c-TiO_2/Sb doped Perovskite/Spiro-OMeTAD/Ag	1.10	22.85	0.84	21.04	+80	[69]
$CsFAPb(I,Br)_3$	FTO/SnO_2/C_{60}-SAM/Perovskite + $Pb(SCN)_2$/Spiro-OMeTAD/Au	1.25	18.53	0.79	18.27	+80	[72]
$CsFAPb(I,Br)_3$	FTO/c-TiO_2/Perovskite/Spiro-OMeTAD/Au	1.07	23.30	0.72	18.02	+60	[70]
$FAMAPb(I,Br)_3$	FTO/c-TiO_2/mp-TiO_2/Perovskite + PMMA/Spiro-OMeTAD/Au	1.14	23.70	0.78	21.60	+40	[73]
$FAMAPb(I,Br)_3$	FTO/c-TiO_2/mp-TiO_2/Perovskite + PCBM/Spiro-OMeTAD/Au	1.13	23.95	0.74	20. 80	+20	[74]
$CsFAMAPb(I,Br)_3$	FTO/c-TiO_2/mp-TiO_2/Perovskite + GuaI/Spiro-OMeTAD/Au	1.20	23.60	0.70	20.30	+70	[77]
$CsFAMAPb(I,Br)_3$	FTO/c-TiO_2/mp-TiO_2/Perovskite + FAAc/Spiro-OMeTAD/Au	1.19	23.23	0.80	21.90	+50	[78]
$MAPb(Cl,I)_3$	ITO/PEIE/Y:TiO_2/Perovskite/ Spiro-OMeTAD/Au	1.15	22.80	0.76	19.30	+110	[79]
$RbCsFAMAPb(I,Br)_3$	FTO/c-TiO_2/CsBr treated mp-TiO_2/Perovskite/Spiro-OMeTAD/Au	1.14	23.20	0.80	21.40	+40	[80]
$FAMAPb(I,Br)_3$	FTO/SnO_2/Perovskite/Spiro-OMeTAD/Au	1.14	21.30	0.74	18.40	+70	[81]
$CsFAPbI_3$	ITO/EDTA-complexed SnO_2/Perovskite/Spiro-OMeTAD/Au	1.11	24.57	0.79	21.60	+30	[82]
$FAMAPb(I,Br)_3$	FTO/F:TiO_2/Perovskite/Spiro-OMeTAD/Au	1.13	22.92	0.78	20.20	+100	[83]
$MAPb(Cl,I)_3$	ITO/SnO_2/LiF/Perovskite/Spiro-OMeTAD/Au	1.15	21.62	0.74	18.33	+70	[84]
$MAPb(Cl,I)_3$	ITO/SnO_2/PbF_2/Perovskite/Spiro-OMeTAD/Au	1.14	19.05	0.71	15.50	+60	[84]
$CsFAMAPb(I,Br)_3$	FTO/Nb:SnO_2/Perovskite/Spiro-OMeTAD/Au	1.16	22.77	0.75	20.47	+20	[85]
$CsFAMAPb(I,Br)_3$	FTO/c-TiO_2/mp-TiO_2/Perovskite/ADAHI/Spiro-OMeTAD/Au	1.17	24.30	0.77	21.90	+60	[90]
$FAMAPb(I,Br)_3$	ITO/C_{60}-SAM/Perovskite/PDCBT/Ta-WO_x/Au	1.17	22.70	0.80	21.20	+60	[91]

$FAMAPb(I,Br)_3$	FTO/c-TiO_2/mp-TiO_2/Perovskite/1F-PTAA/Au	1.14	23.40	0.82	22.00	+40	[92]
$FAMAPb(I,Br)_3$	FTO/c-TiO_2/mp-TiO_2/Perovskite/DM/Au	1.14	24.91	0.81	23.20	+70	[93]
$MAPb(Cl,I)_3$	FTO/NiO/DEA/Perovskite/PCBM/PN4N/Ag	0.95	20.90	0.80	15.90	0	[96]
$CsFAMAPb(I,Br)_3$	ITO/F6TCNNQ:NiO_x/Perovskite/PCBM/ZrAcac/Ag	1.12	23.18	0.80	20.86	+50	[97]
$FAMAPb(I,Cl)_3$	FTO/NiO/Perovskite/PCBM/BCP/Ag	1.12	23.70	0.76	20.20	+60	[98]
$MAPb(I,Br)_3$	ITO/GO:Pedot/Perovskite/PCBM/ZnO/Ag	1.02	21.55	0.82	18.09	+50	[99]
$CsFAMAPb(I,Br)_3$	ITO/PTAA/PFN-P2/Perovskite/LiF/C_{60}/Au	1.17	21.70	0.79	20.30	+50	[100]
$RbCsFAMAPb(I,Br)_3$	FTO/In-TiO_x/mp-TiO_2/PMMA/Perovskite/PMMA/Spiro-OMeTAD/Au	1.17	22.75	0.76	20.28	+60	[101]
$CsFAMAPb(I,Br)_3$	FTO/c-TiO_2/mp-TiO_2/Perovskite/$CsPb(Br,I)_3$/Au	1.14	23.42	0.79	21.14	+50	[102]
$CsFAMAPb(I,Br)_3$	FTO/Ru:SnO_2/Perovskite/Spiro-OMeTAD/Au	1.15	24.58	0.78	22.00	+50	[103]
$MAPb(Br,I)_3$	ITO/PTAA/Perovskite /PCBM/C_{60}/BCP/Al	1.21	15.80	0.78	14.90	+50	[104]
$CsFAMAPb(I,Br)_3$	ITO/Chlorine-capped c-TiO_2/Perovskite/Spiro-OMeTAD/Au	1.22	21.20	0.81	20.80	+50	[105]
$CsFAMAPb(I,Br)_3$	ITO/SnO_2/Perovskite:NaF/Spiro-OMeTAD/Au	1.13	24.23	0.80	21.92	+30	[106]
$CsFAMAPb(I,Br)_3$	ITO/PTAA/Perovskite/D4TBP /C_{60}/BCP/Cu	1.16	22.51	0.80	21.40	+80	[107]
$CsFAPb(I,Br)_3$	ITO/PTAA/Perovskite + GABr/C_{60}/BCP/Ag	1.24	21.72	0.72	18.19	+120	[108]
$CsFAPb(I,Br)_3$	FTO/SnO_2/PCBM/Perovskite/Spiro-OMeTAD/Ag	1.20	19.40	0.75	17.10	+100	[109]
$CsFAMAPb(I,Br)_3$	ITO/TiO_2-cl/PbI_2 seed/Perovskite/Spiro-OMeTAD/Au	1.13	24.10	0.81	21.50	+60	[110]
$FAMAPb(I,Br)_3$	FTO/c-TiO_2/mp-TiO_2/Perovskite/$FAPbBr_{3-x}I_x$/Spiro-OMeTAD/Au	1.16	23.18	0.79	21.31	+50	[111]
$CsFAMAPb(I,Br)_3$	FTO/SnO_2/Zwitterion/Perovskite/Spiro-OMeTAD/Au	1.16	23.60	0.78	21.43	+60	[112]
$FAMAPb(I,Br)_3$	FTO/c-TiO_2/mp-TiO_2/Perovskite/G2/Au	1.13	23.52	0.76	20.20	+50	[113]

4. LD/3D-based perovskites

Low-dimensional (LD = 1D, 2D) perovskites have witnessed a great development in terms of long-term stability under external conditions owing to the effective protection by the hydrophobic organic spacing-ligands.[114,115] However, because of their wide optical bandgaps and anisotropic charge transport properties caused by the long organic spacing-ligand, the *PCE* of pure LD based PSCs is still far inferior to their 3D analogues.[115,116,117] To marry the desired features of LD perovskites with the excellent light-harvesting properties of 3D perovskite, LD systems have recently emerged as a potential candidate to simultaneously maintain long-term stability and high photovoltaic performance. In the following section, the substantial role of LD perovskites within a 3D dominant structure either as an additive or as overlayer is discussed.

The confluence of high-efficiency 3D perovskites with superior moisture stability of LD perovskite absorbers has recently ignited quiet interest in the concept of LD-3D hetero-structured PSCs. Hu *et al*. were the first to propose the two-layer approach in 2D/3D ($(PEA)_2(MA)_4Pb_5I_{16}$/$MAPbI_3$) heterojunction-based PSCs.[118] Grazing-incidence wide-angle X-ray scattering (GIWAXS) pattern revealed the preferential orientation of the layered 2D perovskite, which is accompanied by a re-organization and re-orientation of the $MAPI_3$ top layer. In the presence of 2D layer, the best-performing devices showed a *PCE* of 14.94% (J_{SC} = 18.63 mA cm^{-2}, V_{OC}= 1.08 V, and *FF*= 0.73), whereas pure 3D-based best-performing devices showed a *PCE* of 13.61% (J_{SC} = 19.82 mA cm^{-2}, V_{OC}= 0.99 V, and *FF*= 0.70). The significant increase in V_{OC} and *FF* was ascribed to reduced recombination losses within the device, inferring the selective charge extraction role of the 2D layer. Such a configuration also provided an additional moisture barrier for the under-3D layer, thus improving the long-term moisture stability owing to the hydrophobic nature of long-chain organic cations. The 2D/3D

perovskite devices exhibited a higher average *PCE* of 11.4%, whereas the 3D perovskite device showed only 6.1% after 19 days of ageing at 75% RH.

Following this work, another 2D/3D hybrid structure was reported on the incorporation of *n*-butylammonium (BA) within the cesium-formamidinium lead halide 3D perovskite $FA_{0.83}Cs_{0.17}Pb(I_yBr_{1-y})_3$ (**Figure 10a**).[119] BA cations facilitated the formation of perpendicularly orientated 2D-phase perovskite crystallites in plate-like morphology embedded between the 3D perovskite grains. This heterostructure enhanced crystallinity and at the same time, interfacial grain boundary passivation remarkably reduced the defect states, leading to an increase in the PL lifetime, higher *PCE*, minimal current-voltage hysteresis, and improved operational stability. A champion stabilized *PCE* of 19.5% and 17.3% was achieved with a 1.61 eV bandgap perovskite (y = 0.8) and a 1.72 eV bandgap (y = 0.6) perovskite, respectively.

Recently, our group presented a method of depositing 2D material onto a bulk 3D perovskite layer to fabricate exceptionally moisture-resistant PSCs with a record-level *PCE* exceeding 22%.[1] In this study, pentafluoro-phenylethylammonium (FEA) lead iodide [$(FEA)_2PbI_4$] 2D perovskite layer was inserted between the 3D perovskite layer and HTM. XPS depth profiling of fluorine (F) confirmed the presence of FEA^+ in the top ~9-nm-thin layer, whereas the EDS mapping showed the conformal and uniform distribution of FEA^+ over the 3D film. The perfluorinated benzene unit bestowed an ultra-hydrophobic character to the FEA spacer layer, protecting the perovskite light absorber from ambient moisture while simultaneously inhibiting interlayer ionic diffusion in the device. The 3D/2D fluoroarene bilayer-based champion PSCs achieved a *PCE* as high as 22.2% with a V_{OC} of 1.096 V, *FF* of 0.79, and J_{SC} of 25.8 mA cm^{-2} while the reference PSC yielded a *PCE* of 20.6% with V_{OC} of 1.045 V, *FF* of 0.78, and J_{SC} of 25.5 mA cm^{-2} (**Figure 10b**). The ~50 mV increase in V_{OC} was attributed to a two-fold increase in the charge carrier lifetime and faster hole injection into the

HTM, implying the suppression of non-radiative carrier recombination at the (3D/2D) perovskite/HTL interface as depicted in **Figure 10c**. In addition, the operational photo-stability was also enhanced by applying the 2D treatment.

More recently, different types of ammonium salts, namely ethylammonium iodide (EAI), imidazolium iodide (IAI), and guanidinium iodide (GuaI) have been introduced to reduce the electronic defects at perovskite/HTL interface.[120] This facile strategy thoroughly modified the triple-cation perovskite surface and showed an improvement in V_{OC} by 40 mV (EAI), 70 mV (IAI), and 40 mV (GuaI), leading to the realization of PCEs as high as 22.4%, 22.1%, and 21.0% for EAI, IAI, and GuaI employed perovskite devices, respectively. The increase in PL intensity for all treated perovskite films further confirmed the reduction of the non-radiative recombination losses that could be explained by defect passivation induced by cation exchange and filling of iodide vacancies at the absorber surface.

In addition to identifying new LD perovskite materials for their integration onto 3D perovskite film, equally important is the preparation of LD perovskite materials. Yoo *et al*. investigated the role of polar protic solvent isopropyl alcohol (IPA) in surface treatments and reported a selective precursor dissolution (SPD) strategy using *n*-butylammonium bromide/chloroform combination for depositing LD layered perovskite onto a 3D perovskite film.[121] It was observed that IPA solvent can dissolve the 3D perovskite in a short time (> 2 s) due to its highly polar nature and its tendency to form hydrogen bonds while non-hygroscopic chloroform showed no change in optical profile. Through this approach, a champion *PCE* of 23.4% (a certified *PCE* of 22.6%) with a V_{OC} loss of only ~340 mV was achieved. The improved *PCE* was ascribed to the effective passivation of interfaces and grain boundary defects. Apart from the stack-by-stack method, the hybridization is another way to prepare LD/3D PSCs. Zhou *et al*. demonstrated that 2-thiophenemethylammonium (ThMA) as the spacer cations can be successfully embedded into the FAI and MAI based 3D

perovskite (**Figure 11a**).[122] The incorporation of ThMA spacer cation into 3D perovskite, forming a 2D/3D hybrid structure accelerated crystalline growth and orientation with enlarged grain size, resulting in prolonged carrier life-time and decreased recombination losses. The 2D/3D hybrid perovskite-based device exhibited a *PCE* of 21.49% with a high V_{OC} of 1.16 V and a significant *FF* of 0.81. This outstanding *FF* was attributed to more balanced charge mobility whereas improved crystallinity, leading an efficient charge collection can explain relatively higher V_{OC}.

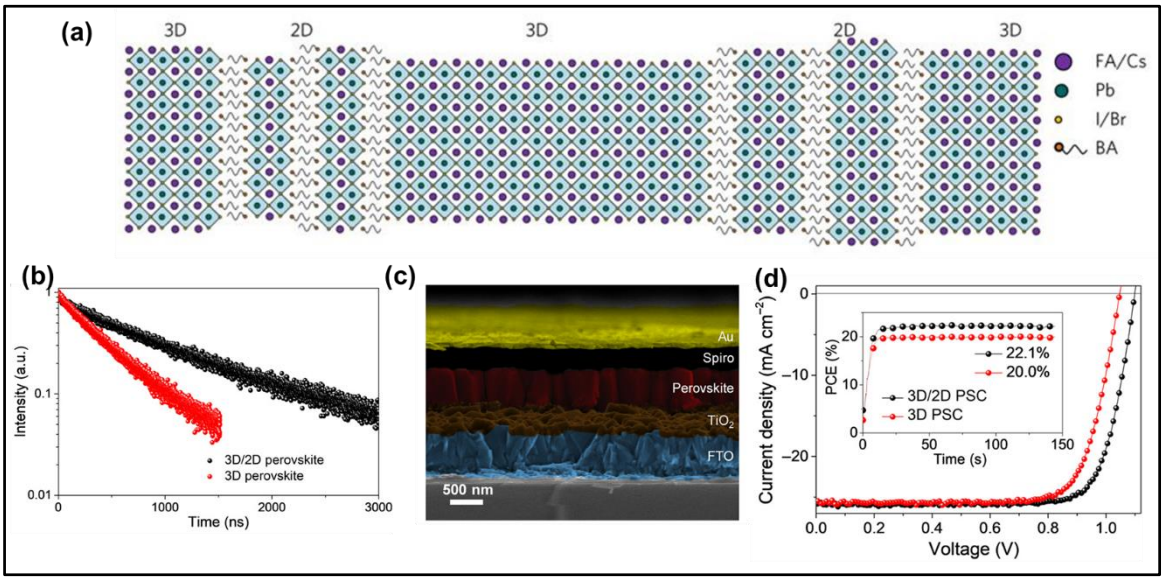

Figure 10. a) Schematic illustration of the proposed self-assembled $BA_{0.09}(FA_{0.83}Cs_{0.17})_{0.91}Pb(I_{0.6}Br_{0.4})_3$, 2D-3D crystal interface. Reproduced with permission.[119] Copyright 2017, Nature Publishing Group. **b)** TRPL decay traces recorded from the 3D and 3D/2D perovskite films showing more than twofold increase in the charge carrier lifetime by applying the 2D surface treatment [t_{10}(3D/2D) = 2550 ns and t_{10}(3D) = 950 ns]. Reproduced under the terms of the CC-BY-NC 4.0 license [1] Copyright 2019, American Association for the Advancement of Science. **c)** Cross-sectional SEM of a fully assembled 3D/2D PSC. Reproduced under the terms of the CC-BY-NC 4.0 license [1] Copyright 2019, American Association for the Advancement of Science. **d)** J-V curves of 3D PSC and 3D/2D PSCs recorded under standard AM 1.5G illumination (100 mW cm^{-2}), with inset showing MPP tracking. Reproduced under the terms of the CC BY-NC 4.0 license [1] Copyright 2019, American Association for the Advancement of Science.

Along this direction, 1-year stable PSCs have been developed by engineering a multidimensional junction made of 2D/3D $(HOOC(CH_2)_4NH_3)_2PbI_4/MAPbI_3$

perovskites.[123] The 2D/3D structure was formed by mixing at different molar ratios of aminovaleric acid iodide ($COOH(CH_2)_4NH_3I$), AVAI: PbI_2) and (CH_3NH_3I: PbI_2) precursors. Both small area cells (0.64 cm^2) and larger area modules (10 × 10 cm^2) were fabricated. For the small area devices, the perovskite employing 3% AVAI formed a gradually-organized multi-dimensional interface that allowed to obtain 12.9% efficiency in a carbon-based architecture and 14.6% in mesoporous device architecture. The module of 100 cm^2 (active area of around 50 cm^2) retained a remarkable air-stability by maintaining a *PCE* of 11.2% over 10 000 h (≈1 year) with zero loss at a stabilized temperature of 55 °C under AM 1.5G conditions under short-circuit conditions.

2D perovskite approach has been also explored in the inverted PSCs with planar architecture using solvent engineering method. Bai *et al*. developed a solution process based in situ growth route to form a 2D capping layer together with 3D perovskite.[124] In this method, phenethylammonium iodide (PEAI) dissolved in toluene solution was used as anti-solvent instead of pure toluene which allowed the formation of 2D capping layer together with 3D perovskite. A 3D-2D ($MAPbI_3$-$PEA_2Pb_2I_4$) graded perovskite layer improved interfacial charge transfer as a result of the modified interface energy level and reduced charge-carrier recombination at the perovskite/PCBM interface (**Figure 11b**). It was described that this graded layer not only enhanced the moisture stability by abating water penetration but also improved the thermal stability by suppressing the ion migration across the interfaces.

In another interesting study, Luo *et al*. described a simple solution-processed secondary growth (SSG) technique to reduce the non-radiative recombination for the inverted devices.[125] This method comprises two sequential steps: the preparation of perovskite films by solution processing and the secondary growth with the assistance of guanidinium bromide (SSG-G). This strategy produced a more *n*-type perovskite film with a wider bandgap top

layer achieving a high V_{OC} of 1.21 V, which was attributed to reduced non-radiative recombination for the $(FA_{0.95}PbI_{2.95})_{0.85}(MAPbBr_3)_{0.15}$ based inverted devices (**Figure 11c**). The presence of guanidinium bromide throughout the films and at the surfaces inhibited undesired trap-assisted recombination at the heterojunctions by trap passivation and considerable improvements in film quality and electronic nature facilitated to obtain a stabilized *PCE* close to 21%.

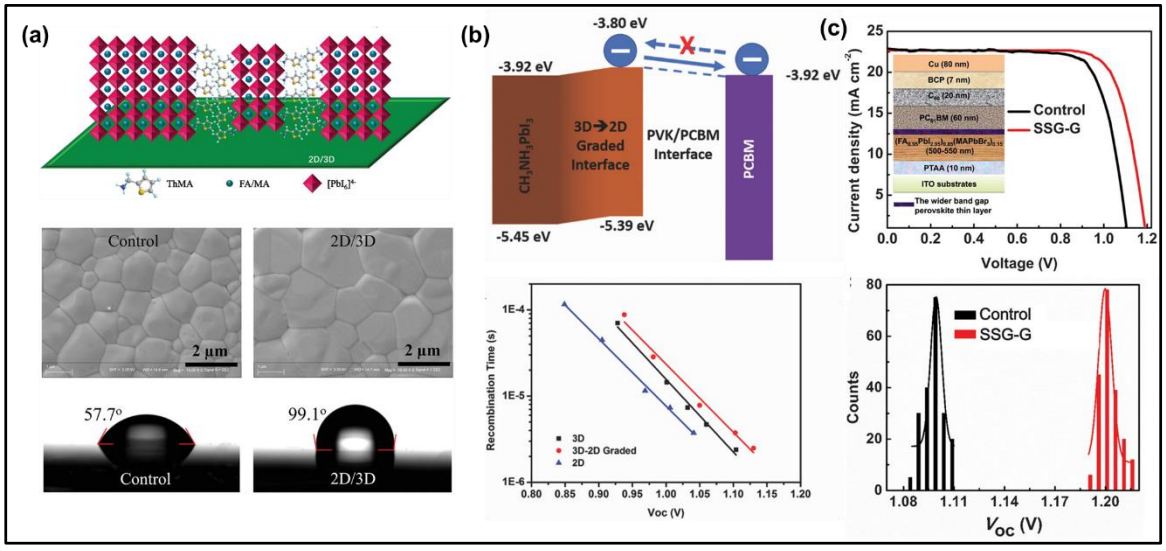

Figure 11. a) Schematic illustration of the proposed 2D/3D perovskite structure, showing the incorporation of large organic cation, ThMAI into the 3D perovskite and formation of 2D layer aligned perpendicular to the substrates, SEM images of the 2D/3D perovskite film on the glass/SnO_2 substrate, and water droplet contact angles on surfaces of the control and the 2D/3D perovskite films. Reproduced with permission.[122] Copyright 2019, John Wiley & Sons. **b)** Schematic illustration of energy level alignment at 3D–2D graded perovskite and PCBM interface and voltage-dependence of recombination lifetime for the different devices. Reproduced with permission.[124] Copyright 2017, John Wiley & Sons . **c)** *J-V* curves of the inverted planar heterojunction control and SSG-G PSCs (reverse scans under simulated AM 1.5G illumination at 100 mW cm^{-2}) and histograms of the V_{oc} for 200 control and 200 SSG-G devices, the average V_{oc} of the control devices was about 1.10 V and 1.20 V for the SSG-G devices, with a record value of 1.21 V. Reproduced with permission.[125] Copyright 2018, American Association for the Advancement of Science.

Table 3 summarizes the recent progress on the photovoltaic performance of LD/3D-based perovskite devices. This field is less matured than the field of pure 3D perovskites, and retaining PCEs comparable to 3D-absorber based PSCs while achieving high operational

stability is still a challenge. Nevertheless, this field is on an interesting trajectory, which is expected to play a substantial role towards stable and efficient devices for industrial applications.

Table 3. V_{OC} and other photovoltaic parameters of LD/3D-based PSCs.

3D perovskite composition	Device configuration	*Voc* (V)	*Jsc* (mA cm^{-2})	*FF*	*PCE* (%)	Change in *Voc* (mV)	Ref.
$Cs_{0.05}(FA_{0.10}MA_{0.90})_{0.95}PbI_3$	FTO/c-TiO_2/mp-TiO_2/3D/$(FEAI)_2PbI_4$/Spiro-OMeTAD/Au/MgF_2	1.10	25.79	0.79	22.16	+50	[1]
$MAPbI_3$	FTO/c-TiO_2/3D/$(PEA)_2(MA)_4Pb_5I_{16}$/Spiro-OMeTAD/Au	1.08	18.63	0.73	14.94	+90	[118]
$FA_{0.83}Cs_{0.17}Pb(I_{0.8}Br_{0.2})_3$	FTO/SnO_2/$PC_{61}BM$/3D + BAI/Spiro-OMeTAD/Au	1.14	22.70	0.80	20.60	0	[119]
$FA_{0.83}Cs_{0.17}Pb(I_{0.6}Br_{0.4})_3$	FTO/SnO_2/$PC_{61}BM$/3D + BAI/Spiro-OMeTAD/Au	1.18	19.80	0.73	17.20	+40	[119]
$(FAPbI_3)_{0.92}(MAPbBr_3)_{0.08}$	FTO/c-TiO_2/mp-TiO_2/3D/$(C_6H_{13}NH_3)_2PbBr_2I_2$/Spiro-OMeTAD/Au	1.16	24.50	0.82	23.40	+50	[121]
$FA_{0.83}MA_{0.17}Pb(I_{0.8}Cl_{0.2})_3$	ITO/SnO_2/3D + ThMAI/Spiro-OMeTAD/MoO_3/Ag	1.16	22.88	0.81	21.49	+70	[122]
$MAPbI_3$	FTO/c-TiO_2/mp-TiO_2/3D + AVAI/Spiro-OMeTAD/Au	1.03	18.84	0.76	14.60	-30	[123]
$MAPbI_3$	FTO/NiO/3D+$PEA_2Pb_2I_4$/PCBM/PN4N/Ag	1.17	21.80	0.78	19.89	+70	[124]
$(FA_{0.95}PbI_{2.95})_{0.85}(MAPbBr_3)_{0.15}$	ITO/PTAA/3D/Gua_2PbBr_4/PCBM/C_{60}/BCP/Cu	1.18	21.86	0.81	20.90	+100	[125]
$Cs_{0.1}FA_{0.74}MA_{0.13}PbI_{2.48}Br_{0.39}$	FTO/c-TiO_2/mp-TiO_2/3D/$A43_2PbI_4$/Spiro-OMeTAD/Au	1.13	22.85	0.78	20.00	+15	[126]
$FA_{0.9}Cs_{0.07}MA_{0.03}Pb(I_{0.92}Br_{0.08})_3$	FTO/c-TiO_2/mp-TiO_2/3D/EAI/Spiro-OMeTAD/Au	1.12	24.14	0.81	22.40	+40	[120]
$FA_{0.9}Cs_{0.07}MA_{0.03}Pb(I_{0.92}Br_{0.08})_3$	FTO/c-TiO_2/mp-TiO_2/3D/IAI/Spiro-OMeTAD/Au	1.15	23.85	0.79	22.11	+70	[120]
$FA_{0.9}Cs_{0.07}MA_{0.03}Pb(I_{0.92}Br_{0.08})_3$	FTO/c-TiO_2/mp-TiO_2/3D/GuaI/Spiro-OMeTAD/Au	1.12	24.50	0.75	21.00	+40	[120]
$MA_{0.9}FA_{0.1}PbI_3$	FTO/c-TiO_2/mp-TiO_2/3D + $A43_2I$/Spiro-OMeTAD/Au	1.11	22.87	0.79	20.13	+70	[126]
$FA_{0.98}Cs_{0.02}PbI_3$	ITO/SnO_2/3D + PEAI/Spiro-OMeTAD/Ag	1.13	24.44	0.77	21.06	+80	[127]

$Cs_{0.1}FA_{0.74}MA_{0.13}PbI_{2.48}Br_{0.39}$	FTO/c-TiO_2/mp-TiO_2/3D/PEA_2PbI_4/Spiro-OMeTAD/Au	1.15	22.73	0.79	20.75	+50	[128]
$FA_{0.15}Cs_{0.85}Pb(I_{0.73}Br_{0.27})_3$	FTO/c-TiO_2/3D/BA_2PbI_4/Spiro-OMeTAD/Au	1.24	19.83	0.74	18.13	+80	[129]
$FA_{0.83}Cs_{0.17}Pb(I_{0.6}Br_{0.4})_3$	ITO/SnO_2/3D/BA_2PbBr_4/Spiro-OMeTAD/Au	1.31	18.40	0.78	19.40	+80	[130]
$Cs_{0.05}(FA_{0.83}MA_{0.17})_{0.95}Pb(I_{0.83}Br_{0.17})_3$	FTO/c-TiO_2/mp-TiO_2/3D/ PEA_2PbI_4/Spiro-OMeTAD/Au	1.11	22.89	0.73	18.51	+60	[131]
$MAPbI_3$	ITO/PTAA/3D/$(BA)_2PbI_4$/PCBM/C_{60}/ BCP/Cu	1.11	22.49	0.78	19.56	+30	[132]

5. Long-term Stability

Besides efficiency, long-term stability is warranted for up-scaling of perovskite technology. The stability of perovskite devices strongly depends on the stability of individual components within the device architecture such as the absorber layer, charge transporting layers, and metal contacts. Therefore, the stability of each component and interfaces is of great importance for commercialization. Thus far, PSC research has bloomed into a race to develop not only efficient but also long-term stable device components. In the following section, the recent advances towards limiting the extrinsic (environmental) and intrinsic factors affecting the device stability have been summarized.

5.1. Operational stability

Among all the promising techniques, additive engineering has been widely applied as an effective and feasible approach to obtaining high-quality perovskite films, thereby leading to enhanced stability of PSCs.

Cesium cation (Cs^+) employing triple-cation perovskite-based devices have displayed improved stability under the operational conditions with an output power of 18% after 250 h while Cs-free perovskite-based devices showed less stable behaviour. [21] In addition to appropriate Goldschmidt tolerance factor, reduced defect states, and the critical role of Cs^+ to mitigate phase separation; the strong interaction of Cs^+ with the lead iodide (or bromide)

octahedral framework greatly improved the photo-stability.[133] Consequently, the incorporation of small and oxidation-stable rubidium cation (Rb^+) into perovskite has further improved the performance and stability of PSCs.[22]

Very recently, a great enhancement in the long-term device stability of inverted type PSCs was reported by the incorporation of ionic liquid, 1-butyl-3-methylimidazolium tetrafluoroborate ($BMIMBF_4$) into the perovskite film.[134] Interestingly, as shown in **Figure 12a**, the encapsulated cells based on $BMIMBF_4$-incorporated perovskite film showed less degradation (< 5%) in comparison to solar cells based on $BMIMBF_4$ at the perovskite/NiO interface, which degraded at a similar rate to the control cells under full solar spectrum after aging at the elevated temperature (70–75 °C). It was envisaged that improved stability originates from the presence of $[BMIM]^+$ cations, that binds to the surface sites and evading degradation.

In the same direction, the formation of thin and compact lead oxysalt on the metal halide perovskite surface was demonstrated by in situ reaction of perovskite with inorganic anions.[135] Such water-insoluble wide-bandgap lead oxysalt thin layers improved the moisture resistance of the perovskite films by forming strong chemical bonds and reducing defect-nucleating sites on the perovskite surface by passivating undercoordinated lead centers. A *PCE* of 21.1% was achieved as a result of the increased carrier recombination lifetime by the formation of lead oxysalt layer as a result encapsulated devices retained 96.8% of their initial efficiency after operation at MPP tracking under continuous illumination for 1200 h at 65°C. Under the same ageing conditions, encapsulated control device degraded rapidly from 18.2% to 8.54% merely in ~470 h. More recently, another solution-processing strategy to stabilize the perovskite heterostructure was reported *via* the formation of strong Pb–Cl and Pb–O chemical bonds in a $[CH(NH_2)_2]_x[CH_3NH_3]_{1-x}Pb_{1+y}I_3$ perovskite film with a Pb-rich surface and a chlorinated graphene oxide (Cl-GO) layer.[136] A reduction in charge recombination and

more-efficient charge extraction in the perovskite/Cl-GO/PTAA heterostructure was revealed by transient photocurrent decay and photovoltage decay measurements. The PSC with the heterostructure of perovskite/Cl-GO maintained 90% of its initial efficiency of 21% at the MPP under AM1.5G solar light at 60°C after 1000 h.

A major bottleneck delaying the further commercialization of PSCs is interfacial losses within the devices. In order to minimize these losses in PSCs, it is essential to decrease the energy barriers within charge-transporting interfaces. Hou *et al*. showed that tantalum-doped tungsten oxide (Ta-WO_x) interlayer can form almost ohmic contacts with polythiophene derivative conjugated polymer multilayers to create an HTL with a small interface barrier.[91] Ta-WO_x/PDCBT (poly[5,5′-bis(2-butyloctyl)-(2,2′-bithiophene)-4,4′-dicarboxylate-alt-5,5′-2,2′-bithiophene]) multilayer based ionic dopant-free approach showed a stabilized *PCE* of 21.2% and almost 95% of its initial efficiency was retained over 1000 h under continuous illumination as depicted in **Figure 11b**.

The poor device stability of traditional HTL of spiro-OMeTAD mainly comes from the highly hydrophilic bis(trifluoromethylsulfonyl)imide (Li-TFSI) dopant, which is indispensable in the case of spiro-OMeTAD owing to its intrinsically low hole mobility. Seo *et al*. introduced a new *p*-type material, namely Zn-$TFSI_2$, to combat the instability issue of spiro-OMeTAD.[89] As compared to Li-TFSI, the utilization of Zn-$TFSI_2$ dopant into spiro-OMeTAD increased the hole mobility of HTL. Besides outstanding efficiency (stabilized *PCE* of 22.0%), the devices employing Zn-$TFSI_2$ exhibited superb photo-stability, showing even a 2% increase in the *PCE* after 600 h of light soaking under continuous illumination at the MPP, while the Li-TFSI based control device degraded severely under similar conditions. Zn-$TFSI_2$ also demonstrated a stable behaviour even under the thermal stress at 50 ^oC and in a humid environment (relative humidity of 40-50%). The approved stability was ascribed to the

non-migration behaviour of zinc ions in the HTL and induced strong electrostatic interaction within the spiro-OMeTAD matrix that suppressed perovskite degradation.

Another promising solution for stabilizing PSCs is the appropriate choice of inorganic based HTLs. Removing the organic HTLs has already been demonstrated to be a very effective approach towards prolonged device stability. Among the various inorganic based HTLs, copper thiocyanate (CuSCN) has been actively pursued by researchers. Improvement of the photovoltaic performance from 12.4% to the very recent achievement over 20% was reported for CuSCN based PSCs.[137,138]

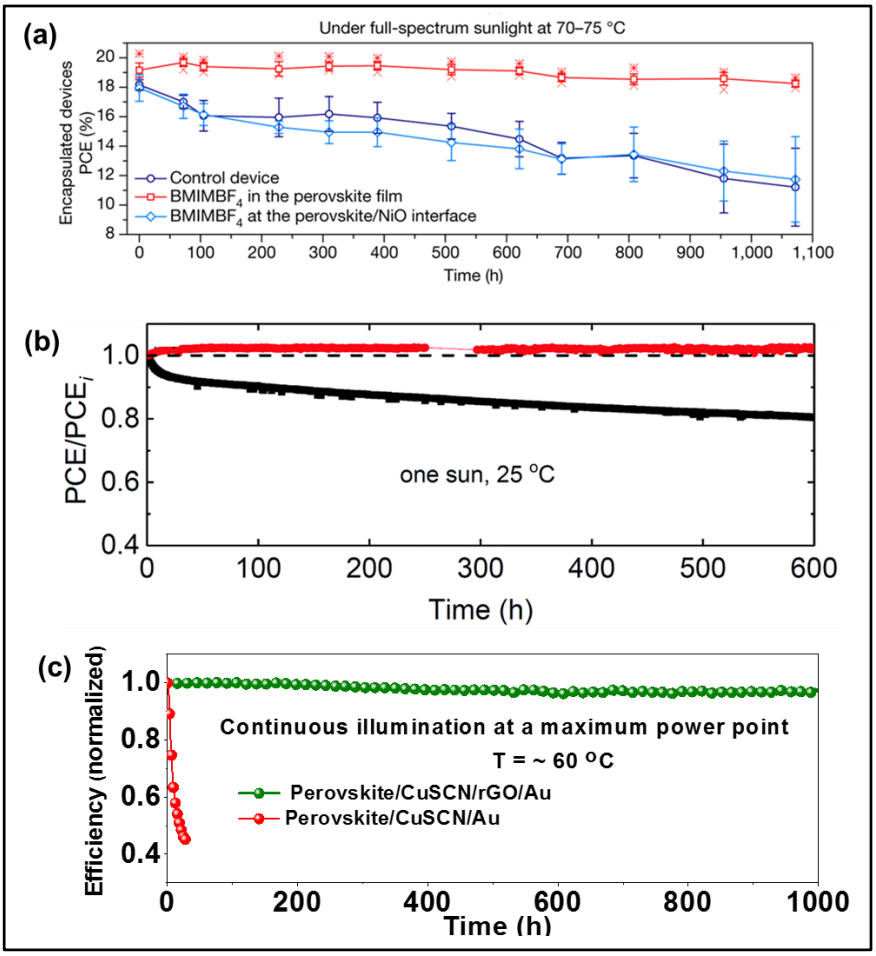

Figure 12. a) Evolution of device stability of the encapsulated control device and a device with $BMIMBF_4$ in the perovskite film and at the perovskite/NiO interface under full-spectrum sunlight at 70-75 °C. Reproduced with permission.[134] Copyright 2019, Nature Publishing Group. **b)** Long-term stability of devices with respect to the dopant for spiro-OMeTAD in the presence of Li-TFSI (black) and Zn-$TFSI_2$ (red) kept at the MPP under continuous one sun illumination (100 mW cm^2) in an inert atmosphere (N_2) at 25 °C. Reproduced with

permission.[89] Copyright 2018, Royal Society of Chemistry. **(c)** Operational stability of an unencapsulated CuSCN-based device with and without a thin layer of rGO, examined at MPP under continuous illumination at 60°C. Reproduced with permission.[139] Copyright 2017, American Association for the Advancement of Science.

Recently, our group demonstrated a stabilized *PCE* exceeding 20% for CuSCN-based devices using a regular architecture.[139] For the first time, it was demonstrated that the instability of PSCs is not associated with the degradation of CuSCN/perovskite interface, but rather arises mainly from the CuSCN/Au contact. By using reduced graphene oxide (rGO) spacer layer between CuSCN and top metal contact,[140] the devices showed a remarkable long-term operational stability retaining >95% of the initial *PCE* after 1000 h under continuous illumination at MPP tracking (T~60 °C) (**Figure 12c**). More recently, a facile and low-cost device architecture employing dopant-free TiO_2 ETL and CuSCN HTL was introduced in which a graphitic carbon (C) layer deposited at room temperature serves as the back electrical contact.[141] The resulting hysteresis-free PSCs reached efficiencies exceeding 18% under standard AM 1.5 solar illumination and retained ~95% of their initial efficiencies after >2000 h at the MPP tracking under full-sun illumination at 60 °C. Moreover, the CuSCN/C-based devices demonstrated a promising UV stability under irradiance for >1000 h while the standard spiro-OMeTAD/Au based devices degraded severely under similar conditions.

5.2. Thermal stability

In addition to the photo-stability, thermal stability is another factor limiting the commercialization of PSCs. As is well known, thermal instability mainly originates from the stability issue of organic molecules, which are necessary to obtain high efficiency.

Choi *et al*. reported a zwitterion-modified SnO_2 ETL for achieving thermally stable and highly efficient planar type PSCs in an inverted architecture.[112] This modification resulted in the formation of interfacial dipoles, shifted the work function of the SnO_2, and

suppressed charge recombination of SnO_2 ETL as depicted in **Figure 13a**. Moreover, the zwitterion passivated the Pb–I antisite traps of the perovskite owing to its positively charged atoms improving the thermal stability of devices. Thermal stability tests were mainly performed in the presence of dopant-free asy-PBTBDT polymer HTL, due to high thermal and moisture sensitivity of doped spiro-OMeTAD. The corresponding devices maintained 82% of their initial *PCE* at 85 ^{o}C and under 85% relative humidity conditions.

In another study, fluorene-terminated N2,N2′,N7,N7′-tetrakis(9,9-dimethyl-9H-fluoren-2-yl)-N2,N2′,N7,N7′-tetrakis(4-methoxyphenyl)-,9′-spirobi[fluorene]-2,2′,7,7′-tetraamine (abbreviated as DM) has been reported as a promising HTL material.[93] The resultant device showed remarkable thermal stability as compared to spiro-OMeTAD employing device, maintaining almost 95% of its initial *PCE* over 500 h thermal annealing at 60 °C. Under identical conditions, the device with spiro-OMeTAD degraded rapidly merely after 50 h (**Figure 13b**). This outstanding thermal stability was attributed to the high glass transition temperature (~160 °C) of the DM material.

As is well known, I^- can be easily oxidized to I^0 and Pb^{2+} is prone to be reduced to metallic Pb^0 upon heating or under illumination and such defects serve not only as recombination centers to deteriorate device performance but also act as degradation initiators to impede the life cycle during the operation. Very recently, Wang *et al*., demonstrated the concurrent oxidation of lead $(Pb)^0$ and reduction of iodine $(I)^0$ defects by rare earth europium ion pair Eu^{3+}-Eu^{2+} acting as the "redox shuttle" in a cyclical transition.[142] In this study, the redox shuttle transferred electrons from Pb^0 to I^0 defects in a cyclic manner, wherein the Eu^{3+} oxidized Pb^0 to Pb^{2+} and the formed Eu^{2+} simultaneously reduced I^0 to I^-. As a result, a considerable *PCE* of 21.5% was obtained with negligible hysteresis. More importantly, the devices retained 92% and 89% of their initial *PCEs*, respectivcely, under the light and thermal stress (at 85°C) for 1500 hours.

5.3. Moisture stability

The degradation of perovskite devices under a humid environment is still a big challenge.[143,144,145] The moisture stability issue, which originates from the hygroscopic nature of methylamine salt and Pb-X framework gets further accelerated in the presence of hygroscopic dopants in HTL material. In recent years, 2D perovskite structures have gained considerable attention owing to their outstanding moisture resistance. Adding a precise amount of 2D material into 3D perovskite or stacking as 2D/3D structure not only improves moisture stability but also suppresses the non-radiative recombination by passivating the surface defect and/or bulk traps of the 3D perovskite.

A 3D/2D hybrid structure using *n*-butylammonium (BA) 2D material within $FA_{0.83}Cs_{0.17}Pb(I_yBr_{1-y})_3$ 3D perovskite was reported.[119] This hybrid structure exhibited enhanced moisture stability in comparison to the control device. The unencapsulated devices were strongly stable at 40% relative humidity over 1000 h and encapsulated devices demonstrated similar features over 3880 h. Very recently, our group reported 2D perovskite layer using pentafluorophenylethylammonium (FEA) as a fluoroarene cation inserted between 3D perovskite and spiro-OMeTAD. **Figure 13c** shows that unsealed 3D/2D PSC retained 90% of its initial efficiency during the photovoltaic operation for 1000 h in humid air under simulated sunlight. In addition to operational stability, we also demonstrated that FEA-based 3D/2D PSC exhibited superior stability in a high relative humidity up to 90%. The excellent moisture resistance of 3D/2D bilayer-based PSCs was attributed to the ultra-hydrophobic character of the perfluorinated 2D perovskite layer.

In addition to the 2D layer, surface modification of the perovskite layer by a functionalized molecule or polymer is another novel strategy to achieve long-term stability against moisture. Hou *et al*. passivated the perovskite surface by introducing oleylammonium

polysulfides (OPs) using dipping treatment to prevent the perovskite layer from erosion by water molecules as shown in **Figure 13d**.[146] The resultant unencapsulated device retained more than 70% of its initial efficiency after 14 days at a relative humidity of 40 ± 10%. The enhanced moisture stability was ascribed to the bulky alkyl chain in OPs assembled by forming Pb-S bond and hydrogen bond, which tighten the OPs-perovskite connection, thus, prevents the perovskite layer from interacting with water molecules. **Table 4** summarizes the recent progress on stability based on different device configurations.

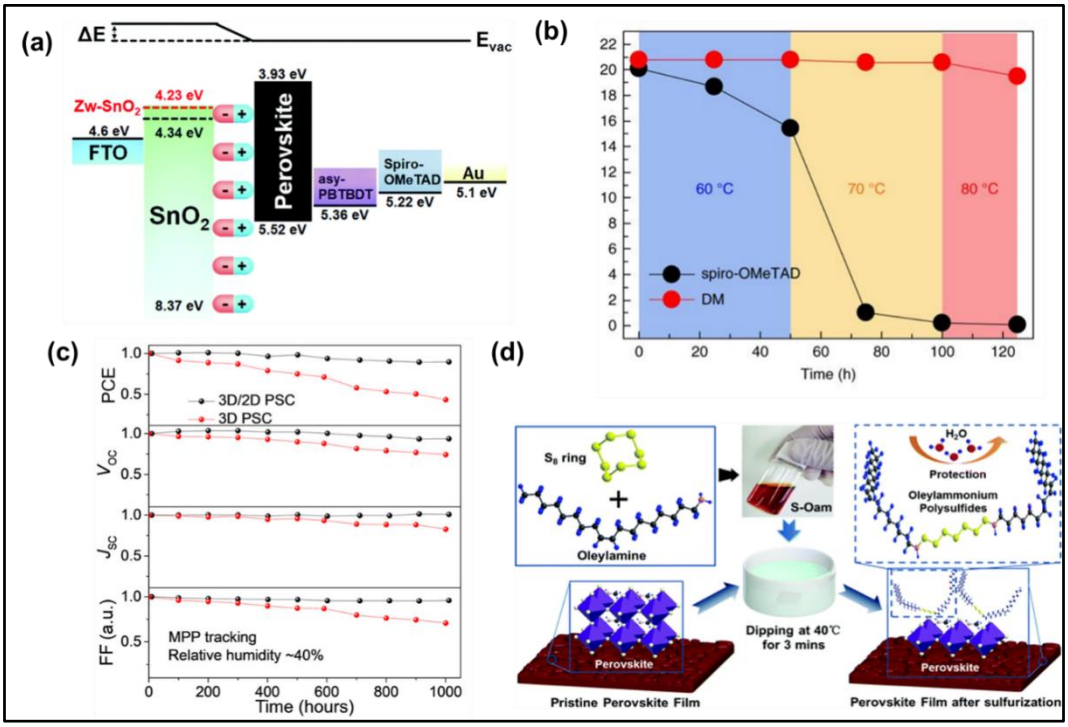

Figure 13. a) Energy diagram of zwitterion (3-(1-pyridinio)-1-propanesulfonate)-modified SnO_2 electron transport layer-based perovskite device. Reproduced with permission.[112] Copyright 2018, Royal Society of Chemistry. **b)** Stability of the devices stressed at different temperatures of 60, 70 and 80 °C in air (~25% RH) with (N^2,$N^{2'}$,N^7,$N^{7'}$-tetrakis(9,9-dimethyl-9H-fluoren-2-yl)-N^2,$N^{2'}$,N^7,$N^{7'}$-tetrakis(4-methoxyphenyl)-9,9′-spirobi[fluorene]-2,2′,7,7′-tetraamine) (DM) and spiro-OMeTAD. Reproduced with permission.[93] Copyright 2018, Nature Publishing Group. **c)** Operational stability of the nonencapsulated devices at the MPP under 1 sun irradiation in ambient condition with a prevalent humidity of 40%for 3D and 3D/2D PSCs. Reproduced under the terms of the CC BY-NC 4.0 license [1] Copyright 2019, American Association for the Advancement of Science. **d)** Schematic representation of the surface modification process with sulfur–oleylamine (S–Oam) solution by H_2S etching and Oleylammonium polysulfides (Ops) assembling on the perovskite surface. Reproduced with permission.[146] Copyright 2019, Royal Society of Chemistry.

These highlighted reports as summarized in **Table 4** show that increasing the device lifetime is a key to the performance of PSCs. It is evident that the aforementioned treatments focusing either on fully assembled -devices (e.g., encapsulation) or on individual components/interfaces within the device have been developed and adopted for PSCs based on different architectures to greatly improve the device longevity. Furthermore, in-depth understanding of the degradation mechanisms is essential for realizing the complete potential of PSCs.

Table 4. V_{OC} and other photovoltaic parameters of highly stable PSCs based on different device configurations.

Measurement conditions	**Device configuration**	***Voc* (V)**	***Jsc* (mA cm^{-2})**	***FF***	***PCE* (%)**	**Change in *Voc* (mV)**	**Degradation rate (%)**	**Ref.**
at MPP, under illumination, humidity of 40%, 1000 h	FTO/c-TiO_2/mp-TiO_2/$CsFAMAPbI_3$ /$(FEAI)_2PbI_4$/spiro-OMeTAD/Au/MgF_2	1.10	25.79	0.79	22.16	+50	-10	[1]
under ambient conditions, 90% humidity, 960 h	FTO/c-TiO_2/mp-TiO_2/$CsFAMAPbI_3$/$(FEAI)_2PbI_4$/spiro-OMeTAD/Au/MgF_2	1.10	25.79	0.79	22.16	+50	-30	[1]
at 85 °C, in a dry box, dark conditions, 60 h	FTO/c-TiO_2/mp-TiO_2/$CsFAMAPbI_3$/$(FEAI)_2PbI_4$/spiro-OMeTAD/Au/MgF_2	1.10	25.79	0.79	22.16	+50	-10	[1]
at MPP, under illumination, 250 h	FTO/c-TiO_2/mp-TiO_2/$CsFAMAPb(I,Br)_3$/spiro-OMeTAD/Au	1.13	22.69	0.75	21.10	+10	-15	[21]
under ambient conditions, 20-25% humidity, 1000 h	FTO/c-TiO_2/$MAPbI_3$+MASCN/spiro-OMeTAD/Au/MgF_2	1.06	22.29	0.77	18.22	+450	-10	[38]
in ambient atmosphere, after 2880 h	ITO/EDTA-complexed SnO_2/$CsFAPbI_3$/spiro-OMeTAD/Au	1.11	24.57	0.79	21.60	+30	-8	[82]
under illumination, 120 h	ITO/EDTA-complexed SnO_2/$CsFAPbI_3$/spiro-OMeTAD/Au	1.11	24.57	0.79	21.60	+30	-14	[82]
at MPP, under illumination, at 60 °C, 500 h	FTO/c-TiO_2/mp-TiO_2/$FAMAPb(I,Br)_3$/DM/Au	1.14	24.91	0.81	23.20	+70	-5	[93]
at MPP, under illumination, 600 h	FTO/c-TiO_2/mp-TiO_2/$CsFAMAPb(I,Br)_3$/spiro-OMeTAD+$Zn(TFSI)_2$/Au	1.15	23.90	0.79	21.50	+50	+2	[89]

at MPP, under illumination, 1000 h	ITO/C_{60}-SAM/FAMAPb(I,Br)$_3$/PDCBT/Ta:WOx/Au	1.17	22.70	0.80	21.20	+60	-5	[91]
at 85 °C, 85% humidity, 140 h	FTO/SnO_2/Zwitterion/CsFAMAPb(I,Br)$_3$/spiro-OMeTAD/Au	1.16	23.60	0.78	21.43	+60	-25	[112]
at 85 °C, 85% humidity, 140 h	FTO/SnO_2/Zwitterion/CsFAMAPb(I,Br)$_3$/PBTBDT/Au	1.14	22.90	0.78	20.50	+40	-5	[112]
at MPP, under illumination, 45% relative humidity, 1000 h	FTO/SnO_2/PC_{61}BM/CsFAPb(I,Br)$_3$+BAI/Spiro-OMeTAD/Au	1.18	19.80	0.73	17.20	+40	-20	[119]
at MPP, under illumination, 45% relative humidity, 3880 h, encapsulated	FTO/SnO_2/PC_{61}BM/FACsPb(I,Br)$_3$+BAI/Spiro-OMeTAD/Au	1.18	19.80	0.73	17.20	+40	-20	[119]
under illumination, 580 h	ITO/SnO_2/$FA_{0.83}MA_{0.17}Pb(I_{0.8}Cl_{0.2})_3$+ThMA/spiro-OMeTAD/$MoO_3$/Ag	1.16	22.88	0.81	21.49	+70	-6	[122]
at 70-75 °C, under illumination, 1800 h	FTO/NiO/$MAPbI_3$+$BMIMBF_4$/PCBM/C_{60}/Cr_2O_3/Au	1.08	23.80	0.81	19.80	+60	-15	[134]
encapsulated, under illumination, ~60 ± 10% humidity, at 65 °C, 1200 h	ITO/PTAA/CsFAMAPb(I,Br)$_3$/C_{60}/BCP/Cu	1.16	22.63	0.80	21.10	+90	-3	[135]
at MPP, under illumination, at 60 °C, 1000 h	ITO/SnO_2/$FAMAPb_{1+y}I_3$/Cl-GO/PTAA/Au	1.12	23.82	0.79	21.08	+30	-10	[136]
at MPP, under illumination, at 60 °C, 1000 h	FTO/c-TiO_2/mp-TiO_2/CsFAMAPb(I,Br)$_3$/CuSCN/rGO/Au	1.11	23.24	0.78	20.40	-20	-5	[139]
at 85 °C, 1500 h	ITO/c-TiO_2/CsFAMAPb(I,Br,Cl)$_3$ + Eu^{3+}-Eu^{2+}/spiro-OMeTAD/Au	1.15	23.53	0.81	21.89	N/A	-11	[142]
under ambient conditions, 30-50% humidity, 14 days	FTO/c-TiO_2/$MAPbI_3$/OPs/spiro-OMeTAD/Ag	1.04	21.90	0.69	15.71	+10	-30	[146]
under illumination, 150 h	FTO/c-TiO_2/$MAPbI_3$/pyridine+spiro-OMeTAD/Au	1.03	20.89	0.69	14.82	+30	-14	[148]
under ambient conditions, 1500 h	FTO/c-TiO_2/$FAMAPbI_3$/thiazole ammonium PbI_3/spiro-OMeTAD/Au	1.08	22.81	0.77	18.97	+50	-8	[147]
in a dry box, dark conditions, 900 h	FTO/c-TiO_2/$MAPbI_3$/pyridine+spiro-OMeTAD/Au	1.03	20.89	0.69	14.82	+30	0	[148]
under ambient conditions, dark storage, 50-	FTO/c-TiO_2/$MAPbI_3$/F4TCNQ/spiro-OMeTAD/Au	1.06	20.30	0.75	16.40	+20	-40	[149]

70% humidity, 960 h								
at MPP, under illumination, 1500 h	FTO/c-TiO_2/mp-TiO_2/CsFAMAPb(I,Br)$_3$/X44/Au	1.08	21.04	0.67	15.20	0	-10	[150]
dark storage, 50% humidity, 7 months	FTO/c-TiO_2/mp-TiO_2/FAMAPb(I,Br)$_3$/BMPyTFSI doped spiro-OMeTAD/Au	1.02	21.17	0.65	14.06	+70	-20	[151]
encapsulated, 40% humidity, under illumination, 500 h	FTO/C_{60}/$MAPbI_3$/[Li^+@C_{60}]$TFSI^-$ doped spiro-OMeTAD/Au	0.89	23.00	0.63	13.10	-80	-20	[152]
under ambient conditions, dark storage, 40% humidity, 120 day	ITO/SnO_2/ODAI modified $FAPbI_3$/spiro-OMeTAD/Au	1.13	24.90	0.75	21.18	+90	-8	[153]
under ambient conditions, dark storage, 95% humidity, 3 months	FTO/c-TiO_2/mp-TiO_2/FAMAPb(I,Br)$_3$/spiro-OMeTAD/Au	1.09	23.23	0.74	18.67	+20	-5	[154]

6. Conclusions and Future Outlook

PSCs hold great promise for the future of solar energy. Although striking progress has been made on the device performance, high requirements with respect to the stability are still a challenge and major efforts are currently directed towards addressing these problems. The primary requirement to achieve remarkably stable efficiencies is to understand in great depth the photo-physics of PSCs. Not only the degradation mechanism of individual layers is important but the optoelectronic loss mechanisms within the device architecture also need to be understood. One of the ways to overcome the current challenges involves the investigation of various engineering approaches such as additive/composition engineering, charge transporting layer engineering, and interface engineering. As discussed above, composition/additive engineering plays a substantial role in obtaining high-efficiency. As compared to single cation-based traditional ($MAPbI_3$) perovskites, multi cation and/or multi halide-based perovskite structures exhibit much desired optoelectronic properties which translate into high device performance. However, the presence of trap states and/or ionic defects still limit the potential of PSC technology.

The meticulous defect healing can be an important strategy to push the efficiency of PSCs to the theoretical limit, as well as to stabilize perovskite-based materials and devices. The design of new molecules to fully passivate the defects on the surface and/or at grain boundaries requires a thorough understanding of the nature, concentration, and distribution of the defects in perovskite devices. Otherwise, defect assisted non-radiative recombination will limit the V_{OC} parameter, thereby, amplify the hysteresis and affect the long-term stability. Furthermore, the mitigation of both non-radiative losses and photoinduced ion migration in perovskite films is vital to obtain higher performance. Towards this direction, interfacial engineering can play a substantial role in reducing the recombination centres and suppressing the ion migration, by decorating the surfaces and grain boundaries with passivating molecules. In addition to suppression of ion migration in the device, the interfacial layer can also prevent the structural phase transitions caused by the degradation induced by moisture, heat, and light.

Another attractive straightforward engineering approach to minimize defects could be the formation of suitable band alignment between high-quality charge-transporting layers and perovskite layer. The rational selection of both ETL and HTL materials can spontaneously eliminate the optoelectronic losses in the devices by transferring the photo-generated charges effectively. Besides, a high-quality charge transporting layer can provide better long-term stability when exposed to moisture, oxygen, thermal stress, UV-light, and forward bias. Furthermore, to boost efficiency and improve the long-term stability beyond the state-of-the-art can be realized by employing stable multi-dimensional hybrid perovskites. The incorporation of an ultra-hydrophobic 2D perovskite materials between hydrophilic 3D perovskite and HTL or ETL could easily mitigate the detrimental charge collection losses. Considering the overall assessment, although device engineering plays a great role to improve efficiency and long-term stability, further investigations are required to reach the

commercialization goals. The innovative engineering approaches to overcome the above-mentioned challenges have been thoroughly summarized and discussed.

Acknowledgements
M.I.D acknowledges financial support from the Swiss National Science Foundation under the project number P300P2_174471. N.A. and R.H.F. thank EPSRC project 'Strategic University Network to Revolutionize Indian Solar Energy-SUNRISE (EP/P032591/1).

Received: ((will be filled in by the editorial staff))
Revised: ((will be filled in by the editorial staff))
Published online: ((will be filled in by the editorial staff))

References

[1] Y. Liu, S. Akin, L. Pan, R. Uchida, N. Arora, J. V. Milić, A. Hinderhofer, F. Schreiber, A. R. Uhl, S. M. Zakeeruddin, A. Hagfeldt, M. I. Dar, M. Grätzel, M. *Sci Adv.* **2019**, *5*, eaaw2543.

[2] W. S. Yang, B.-W. Park, E. H. Jung, N. J. Jeon, Y. C. Kim, D. U. Lee, S. S. Shin, J. Seo, E. K. Kim, J. H. Noh, S. I. Seok, *Science.* **2017**, *356*, 1376-1379.

[3] E. H. Jung, N. J. Jeon, E. Y. Park, C. S. Moon, T. J. Shin, T.-Y. Yang, J. H. Noh, J. Seo, *Nature.* **2019**, *567*, 511-515.

[4] H.-S. Kim, C.-R. Lee, J.-H. Im, K.-B. Lee, T. Moehl, A. Marchioro, S.-J. Moon, R. Humphry-Baker, J.-H. Yum, J. E. Moser, M. Grätzel, N.-G. Park, *Sci Rep*- **2012**, *2*, 591.

[5] M. Abdi-Jalebi, M. Ibrahim Dar, S. P. Senanayak, A. Sadhanala, Z. Andaji-Garmaroudi, L. M. Pazos-Outón, J. M. Richter, A. J. Pearson, H. Sirringhaus, M. Grätzel, R. H. Friend, *Sci. Adv.* **2019**, *5*, eaav2012.

[6] M. M. Lee, J. Teuscher, T. Miyasaka, T. N. Murakami, H. J. Snaith, *Science* **2012**, *338*, 643.

[7] S. De Wolf, J. Holovsky, S.-J. Moon, P. Löper, B. Niesen, M. Ledinsky, F.-J. Haug, J.-H. Yum, C. Ballif, *J Phys Chem Lett.* **2014**, *5*, 1035-1039.

[8] M. I. Dar, G. Jacopin, S. Meloni, A. Mattoni, N. Arora, A. Boziki, S. M. Zakeeruddin, U. Rothlisberger, M. Grätzel,M. *Sci Adv.* **2016**, *2*, e1601156.

[9] G. Xing, N. Mathews, S. Sun, S. S. Lim, Y. M. Lam, M. Grätzel, S. Mhaisalkar, T. C. Sum, *Science.* **2013**, *342*, 344-347.

[10] A. Kojima, K. Teshima, Y. Shirai, T. Miyasaka, *J Am Chem Soc.* **2009**, *131*, 6050-6051.

[11] National Renewable Energy Laboratory (NREL). https://www.nrel.gov/pv/cell-efficiency.html. (accessed August 2019)

[12] T. S. Sherkar, C. Momblona, L. Gil-Escrig, J. Ávila, M. Sessolo, H. J. Bolink, L. J. A. Koster, *ACS Energy Lett.* **2017**, *2*, 1214-1222.

[13] J. Shi, Y. Li, Y. Li, D. Li, Y. Luo, H. Wu, Q. Meng, *Joule.* **2018**, *2*, 879-901.

[14] M. I. Dar, M. Franckevičius, N. Arora, K. Redeckas, M. Vengris, V. Gulbinas, S. M. Zakeeruddin, M. Grätzel, *Chem. Phys. Lett.* **2017**, *683*, 211-215.

[15] A. K. Chandiran, M. Abdi-Jalebi, A. Yella, M. I. Dar, C. Yi, S. A. Shivashankar, M. K. Nazeeruddin, M. Grätzel, *Nano Lett.* **2014**, *14*, 1190-1195.

[16] M. I. Dar, A. Hinderhofer, G. Jacopin, V. Belova, N. Arora, S. M. Zakeeruddin, F. Schreiber, M. Grätzel, *Adv. Funct. Mater.* **2017**, *27*, 1701433.

[17] M. I. Dar, G. Jacopin, M. Hezam, N. Arora, S. M. Zakeeruddin, B. Deveaud, M. K. Nazeeruddin, M. Gratzel, *Acs Photonics.* **2016**, *3*, 947-952.

[18] A. Greco, A. Hinderhofer, M. I. Dar, N. Arora, J. Hagenlocher, A. Chumakov, M. Gratzel, F. Schreiber, *J Phys Chem Lett* **2018**, *9*, 6750-6754.

[19] J.-W. Lee, D.-H. Kim, H.-S. Kim, S.-W. Seo, S. M. Cho, N.-G. Park, *Adv Energy Mater.* **2015**, *5*, 1501310.

[20] D. W. Ferdani, S. R. Pering, D. Ghosh, P. Kubiak, A. B. Walker, S. E. Lewis, A. L. Johnson, P. J. Baker, M. S. Islam, P. J. Cameron, *Energ Environ Sci.* **2019**, *12*, 2264-2272.

[21] M. Saliba, T. Matsui, J.-Y. Seo, K. Domanski, J.-P. Correa-Baena, M. K. Nazeeruddin, S. M. Zakeeruddin, W. Tress, A. Abate, A. Hagfeldt, M. Grätzel, M. *Energ Environ Sci.* **2016**, *9* , 1989-1997.

[22] M. Saliba, T. Matsui, K. Domanski, J.-Y. Seo, A. Ummadisingu, S. M. Zakeeruddin, J.-P. Correa-Baena, W. R. Tress, A. Abate, A. Hagfeldt, M. Grätzel, *Science* **2016**, *354*, 206.

[23] F. Zheng, W. Chen, T. Bu, K. P. Ghiggino, F. Huang, Y. Cheng, P. Tapping, T. W. Kee, B. Jia, X. Wen, *Adv Energy Mater.* **2019**, *9* , 1901016.

[24] a) W. Zhang, J. Xiong, J. Li, W. A. Daoud,. *J Mater Chem A.* **2019**, *7* , 9486-9496. b) M. H. Alotaibi, Y. A. Alzahrani, N. Arora, A. Alyamani, A. Albadri, H. Albrithen, I. H. Al-Lehyani, S. M. Alenzi, A. Z. Alanzi, F. S. Alghamdi, S. M. Zakeeruddin, S. Meloni, M. I. Dar, M. Graetzel, *Solar RRL* **2019**, *0*, 1900234.c) M. Abdi-Jalebi, M. I. Dar, A. Sadhanala, S. P. Senanayak, M. Franckevičius, N. Arora, Y. Hu, M. K. Nazeeruddin, S. M. Zakeeruddin, M. Grätzel, R. H. Friend, *Adv Energy Mater.* **2016**, *6*, 1502472.

[25] Y. Yang, H. Peng, C. Liu, Z. Arain, Y. Ding, S. Ma, X. Liu, T. Hayat, A. Alsaedi, S. Dai, *J Mater Chem A.* **2019**, *7* , 6450-6458.

[26] W. Xiang, Z. Wang, D. J. Kubicki, W. Tress, J. Luo, D. Prochowicz, S. Akin, L. Emsley, J. Zhou, G. Dietler, M. Grätzel, A. Hagfeldt, *Joule.* **2019**, *3*, 205-214.

[27] G. Yang, C. Wang, H. Lei, X. Zheng, P. Qin, L. Xiong, X. Zhao, Y. Yan, G. Fang, *J Mater Chem A.* **2017**, *5*, 1658-1666.

[28] Y. Bai, X. Meng, S. Yang, *Adv Energy Mater.* **2018**, *8*, 1701883.

[29] L. Yan, Q. Xue, M. Liu, Z. Zhu, J. Tian, Z. Li, Z. Chen, Z. Chen, H. Yan, H.-L. Yip, Y. Cao, *Adv Mater.* **2018**, *30*, 1802509.

[30] Cheng, B.; Li, T. Y.; Wei, P. C.; Yin, J.; Ho, K. T.; Retamal, J. R. D.; Mohammed, O. F.; He, J. H *Nat Commun.* **2018**, *9*, 5196.

[31] Li, H.; Wang, X. K.; Zhang, T.; Gong, X.; Sun, Q.; Pan, H.; Shen, Y.; Ahmad, S.; Wang, M. K. *Adv Funct Mater.* **2019**, *29*, 1903293.

[32] Koh, T. M.; Shanmugam, V.; Schlipf, J.; Oesinghaus, L.; Muller-Buschbaum, P.; Ramakrishnan, N.; Swamy, V.; Mathews, N.; Boix, P. P.; Mhaisalkar, S. G. *Adv Mater.* **2016**, *28*, 3653-3661.

[33] C. Roldan-Carmona, C.; Gratia, P.; Zimmermann, I.; Grancini, G.; Gao, P.; Graetzel, M.; Nazeeruddin, M. K. *Energ Environ Sci.* **2015**, *8*, 3550-3556.

[34] F. Li, W. Zhu, C. Bao, T. Yu, Y. Wang, X. Zhou, Z. Zou,. *Chem Commun.* **2016**, *52* (31), 5394-5397.

[35] X. P. Zheng, B. Chen, J. Dai, Y. J. Fang, Y. Bai, Y. Z. Lin, H. T. Wei, X. C. Zeng, J. S. Huang, *Nat Energy.* **2017**, *2*, 17102.

[36] C. G. Wu, C. H. Chiang, Z. L. Tseng, M. K. Nazeeruddin, A. Hagfeldt, M. Gratzel, *Energ Environ Sci.* **2015**, *8* , 2725-2733.

[37] J. B. You, Y. M. Yang, Z. R. Hong, T. B. Song, L. Meng, Y. S. Liu, C. Y. Jiang, H. P. Zhou, W. H. Chang, G. Li, Y. Yang, *Appl Phys Lett.* **2014**, *105*, 183902.

[38] Q. W. Han, Y. S. Bai, J. Liu, K. Z. Du, T. Y. Li, D. Ji, Y. H. Zhou, C. Y. Cao, D. Shin, J. Ding, A. D. Franklin, J. T. Glass, J. S. Hu, M. J. Therien, J. Liu, D. B. Mitzi, *Energ Environ Sci.* **2017**, *10* (11), 2365-2371.

[39] W. R. Zhou, D. Li, Z. G. Xiao, Z. L. Wen, M. M. Zhang, W. P. Hu, X. J. Wu, M. T. Wang, W. H. Zhang, Y. L. Lu, S. H. Yang, S. F. Yang,. *Adv Funct Mater.* **2019**, *29*, 1901026.

[40] Z. F. Liu, L. Kruckemeier, B. Krogmeier, B. Klingebiel, J. A. Marquez, S. Levcenko, S. Oz, S. Mathur, U. Rau, T. Unold, T. Kirchartz, *Acs Energy Lett.* **2019**, *4* , 110-117.

[41] M. Abdi-Jalebi, M. Pazoki, B. Philippe, M. I. Dar, M. Alsari, A. Sadhanala, G. Diyitini, R. Imani, S. Lilliu, J. Kullgren, H. Rensmo, M. Gratzel, R. H. Friend, *Acs Nano.* **2018**, *12*, 7301-7311.

[42] M. Abdi-Jalebi, M. I. Dar, A. Sadhanala, S. P. Senanayak, M. Grätzel, R. H. Friend, *JoVE* **2017**, e55307.

[43] R. Uchida, S. Binet, N. Arora, G. Jacopin, M. H. Alotaibi, A. Taubert, S. M. Zakeeruddin, M. I. Dar, M. Graetzel, *Small* **2018**, *14*, 1802033.

[44] M. T. Klug, A. Osherov, A. A. Haghighirad, S. D. Stranks, P. R. Brown, S. Bai, J. T. W. Wang, X. Dang, V. Bulović, H. J. Snaith, A. M. Belcher, *Energ Environ Sci.* **2017**, *10*, 236-246.

[45] M. Abdi-Jalebi, M. I. Dar, A. Sadhanala, S. P. Senanayak, F. Giordano, S. M. Zakeeruddin, M. Grätzel, R. H. Friend, Impact of a Mesoporous Titania-Perovskite Interface on the Performance of Hybrid Organic-Inorganic Perovskite Solar Cells. *J Phys Chem Lett.* **2016**, *7*, 3264-3269.

[46] Y. Dong, W. Li, X. Zhang, Q. Xu, Q. Liu, C. Li, Z. Bo, *Small.* **2016**, *12*, 1098-1104.

[47] A. Kogo, Y. Sanehira, Y. Numata, M. Ikegami, T. Miyasaka, *Acs Appl Mater Inter.* **2018**, *10*, 2224-2229.

[48] R. Azmi, W. T. Hadmojo, S. Sinaga, C.-L. Lee, S. C. Yoon, I. H. Jung, S.-Y. Jang, *Adv Energy Mater.* **2018**, *8*, 1701683.

[49] Y. Wang, S. Wang, X. Chen, Z. Li, J. Wang, T. Li, X. Deng, *J Mater Chem A.* **2018**, *6* (11), 4860-4867.

[50] S. Wang, H. Chen, J. Zhang, G. Xu, W. Chen, R. Xue, M. Zhang, Y. Li, Y. Li, *Adv Mater.* **2019**, *31*, 1903691.

[51] C. Bi, Q. Wang, Y. Shao, Y. Yuan, Z. Xiao, J. Huang, *Nat Commun.* **2015**, *6*, 7747.

[52] H. D. Pham, T. T. Do, J. Kim, C. Charbonneau, S. Manzhos, K. Feron, W. C. Tsoi, J. R. Durrant, S. M. Jain, P. Sonar, *Adv Energy Mater.* **2018**, *8* , 1703007.

[53] C. M. Wolff, F. Zu, A. Paulke, L. P. Toro, N. Koch, D. Neher, *Adv Mater.* **2017**, *29* , 1700159.

[54] M. Zhong, Y. Liang, J. Zhang, Z. Wei, Q. Li, D. Xu, *J Mater Chem A.* **2019**, *7* (12), 6659-6664.

[55] Z. Liu, S. Li, X. Wang, Y. Cui, Y. Qin, S. Leng, Y.-x. Xu, K. Yao, H. Huang, *Nano Energy*. **2019**, *62*, 734-744.

[56] J. Huang, S. Xiang, J. Yu, C.-Z. Li, *Energ Environ Sci.* **2019**, *12*, 929-937.

[57] G. Xu, R. Xue, W. Chen, J. Zhang, M. Zhang, H. Chen, C. Cui, H. Li, Y. Li, Y. Li, *Adv. Mater. Energy* **2018**, *8*, 1703054.

[58] G. Han, F. Wang, C. Jia, Y. Chen, M. Guan, H. Liu, Q. Zhang, *Mater Chem Phys.* **2018**, *219*, 90-95.

[59] D. Saranin, P. Gostischev, D. Tatarinov, I. Ermanova, V. Mazov, D. Muratov, A. Tameev, D. Kuznetsov, S. Didenko, A. Di Carlo, *Materials.* **2019**, *12* , 1406.

[60] N. Pellet, P. Gao, G. Gregori, T. Y. Yang, M. K. Nazeeruddin, J. Maier, M. Gratzel, *Angew Chem Int Edit.* **2014**, *53*, 3151-3157

[61] N. J. Jeon, J. H. Noh, Y. C. Kim, W. S. Yang, S. Ryu, S. I. Seok, *Nat Mater.* **2014**, *13*, 897-903.

[62] M. I. Dar, N. Arora, P. Gao, S. Ahmad, M. Gratzel, M. K. Nazeeruddin, *Nano Lett.* **2014**, *14*, 6991-6996.

[63] M. I. Dar, M. Abdi-Jalebi, N. Arora, T. Moehl, M. Gratzel, M. K. Nazeeruddin, *Adv Mater.* **2015**, *27*, 7221-7228.

[64] M. I. Dar, M. Abdi-Jalebi, N. Arora, M. Gratzel, M. K. Nazeeruddin, *Adv Energy Mater.* **2016**, *6* , 1501358.

[65] G. Longo, C. Momblona, M. G. La-Placa, L. Gil-Escrig, M. Sessolo, H. J. Bolink, *Acs Energy Lett.* **2018**, *3*, 214-219.

[66] a)C. Huang, P. Lin, N. Q. Fu, C. Liu, B. M. Xu, K. W. Sun, D. Y. Wang, X. R. Zeng, S. M. Ke, *Chem Commun.* **2019**, *55* , 2777-2780. b) J. Huang, M. Wang, L. Ding, Z. Yang, K. Zhang, *RSC Adv* **2016**, *6*, 55720-55725.

[67] Y. Wang, M. I. Dar, L. K. Ono, T. Y. Zhang, M. Kan, Y. W. Li, L. J. Zhang, X. T. Wang, Y. G. Yang, X. Y. Gao, Y. B. Qi, M. Gratzel, Y. X. Zhao, *Science.* **2019**, *36*, 591-595.

[68] C. L. Wang, D. W. Zhao, Y. Yu, N. Shrestha, C. R. Grice, W. Q. Liao, A. J. Cimaroli, J. Chen, R. J. Ellingson, X. Z. Zhao, Y. F. Yan, *Nano Energy.* **2017**, *35*, 223-232.

[69] H. W. Qiao, S. Yang, Y. Wang, X. Chen, T. Y. Wen, L. J. Tang, Q. L. Cheng, Y. Hou, H. J. Zhao, H. G. Yang, *Adv Mater.* **2019**, *31* , 1804217.

[70] C. Y. Yi, J. S. Luo, S. Meloni, A. Boziki, N. Ashari-Astani, C. Gratzel, S. M. Zakeeruddin, U. Rothlisberger, M. Gratzel, *Energ Environ Sci.* **2016**, *9* (2), 656-662.

[71] N. J. Jeon, J. H. Noh, W. S. Yang, Y. C. Kim, S. Ryu, J. Seo, S. I. Seok, *Nature.* **2015**, *517* , 476-480.

[72] Y. Yu, C. L. Wang, C. R. Grice, N. Shrestha, D. W. Zhao, W. Q. Liao, L. Guan, R. A. Awni, W. W. Meng, A. J. Cimaroli, K. Zhu, R. J. Ellingson, Y. F. Yan, *Acs Energy Lett.* **2017**, *2*, 1177-1182.

[73] D. Q. Bi, C. Y. Yi, J. S. Luo, J. D. Decoppet, F. Zhang, S. M. Zakeeruddin, X. Li, A. Hagfeldt, M. Gratzel, *Nat Energy.* **2016**, *1*, 16142.

[74] F. Zhang, W. D. Shi, J. S. Luo, N. Pellet, C. Y. Yi, X. Li, X. M. Zhao, T. J. S. Dennis, X. G. Li, S. R. Wang, Y. Xiao, S. M. Zakeeruddin, D. Q. Bi, M. Gratzel, *Adv Mater.* **2017**, *29*, 1606806.

[75] A. Albadri, P. Yadav, M. Alotaibi, N. Arora, A. Alyamani, H. Albrithen, M. I. Dar, S. M. Zakeeruddin, M. Gratzel, *J Phys Chem C.* **2017**, *121*, 24903-24908.

[76] P. Yadav, M. I. Dar, N. Arora, E. A. Alharbi, F. Giordano, S. M. Zakeeruddin, M. Gratzel, *Adv Mater.* **2017**, *29*, 1701077.

[77] E. A. Alharbi, M. I. Dar, N. Arora, M. Alotaibi, Y. A. Alzhrani, P. Yadav, W. Tress, A. Alyamani, A. Albadri, S. M. Zakeeruddin, M. Grätzel, *Research.* **2019**, *2019*, 8474698.

[78] R. Fu, Y. C. Zhao, W. K. Zhou, Q. Li, Y. Zhao, Q. Zhao, *J Mater Chem A.* **2018**, *6*, 14387-14391.

[79] H. P. Zhou, Q. Chen, G. Li, S. Luo, T. B. Song, H. S. Duan, Z. R. Hong, J. B. You, Y. S. Liu, Y. Yang, *Science.* **2014**, *345*, 542-546.

[80] J. Y. Seo, R. Uchida, H. S. Kim, Y. Saygili, J. S. Luo, C. Moore, J. Kerrod, A. Wagstaff, M. Eklund, R. McIntyre, N. Pellet, S. M. Zakeeruddin, A. Hagfeldt, M. Gratzel, *Adv Funct Mater.* **2018**, *28*, 1705763.

[81] J. P. C. Baena, L. Steier, W. Tress, M. Saliba, S. Neutzner, T. Matsui, F. Giordano, T. J. Jacobsson, A. R. S. Kandada, S. M. Zakeeruddin, A. Petrozza, A. Abate, M. K. Nazeeruddin, M. Gratzel, A. Hagfeldt, *Energ Environ Sci.* **2015**, *8*, 2928-2934

[82] D. Yang, R. X. Yang, K. Wang, C. C. Wu, X. J. Zhu, J. S. Feng, X. D. Ren, G. J. Fang, S. Priya, S. Z. Liu, *Nat Commun.* **2018**, *9*, 3239.

[83] X. Gong, Q. Sun, S. S. Liu, P. Z. Liao, Y. Shen, C. Gratzel, S. M. Zakeeruddin, M. Gratzel, M. K. Wang, *Nano Lett.* **2018**, *18*, 3969-3977.

[84] S. J. Yuan, J. Wang, K. L. Yang, P. F. Wang, X. Zhang, Y. Q. Zhan, L. R. Zheng, *Nanoscale.* **2018**, *10*, 18909-18914.

[85] E. H. Anaraki, A. Kermanpur, M. T. Mayer, L. Steier, T. Ahmed, S. H. Turren-Cruz, J. Y. Seo, J. S. Luo, S. M. Zakeeruddin, W. R. Tress, T. Edvinsson, M. Gratzel, A. Hagfeldt, J. P. Correa-Baena, *Acs Energy Lett.* **2018**, *3*, 773-778.

[86] H. S. Kim, J. Y. Seo, S. Akin, E. Simon, M. Fleischer, S. M. Zakeeruddin, M. Gratzel, A. Hagfeldt, *Nano Energy.* **2019**, *61*, 126-131.

[87] S. Akin, Y. H. Liu, M. I. Dar, S. M. Zakeeruddin, M. Gratzel, S. Turan, S. Sonmezoglu, *J Mater Chem A.* **2018**, *6* , 20327-20337.

[88] J. P. Correa-Baena, W. Tress, K. Domanski, E. H. Anaraki, S. H. Turren-Cruz, B. Roose, P. P. Boix, M. Gratzel, M. Saliba, A. Abate, A. Hagfeldt, *Energ Environ Sci.* **2017**, *10*, 1207-1212.

[89] J. Y. Seo, H. S. Kim, S. Akin, M. Stojanovic, E. Simon, M. Fleischer, A. Hagfeldt, S. M. Zakeeruddin, M. Gratzel, *Energ Environ Sci.* **2018**, *11*, 2985-2992.

[90] M. M. Tavakoli, W. Tress, J. V. Milic, D. Kubicki, L. Emsley, M. Gratzel, *Energ Environ Sci.* **2018**, *11*, 3310-3320.

[91] Y. Hou, X. Y. Du, S. Scheiner, D. P. McMeekin, Z. P. Wang, N. Li, M. S. Killian, H. W. Chen, M. Richter, I. Levchuk, N. Schrenker, E. Spiecker, T. Stubhan, N. A. Luechinger, A. Hirsch, P. Schmuki, H. P. Steinruck, R. H. Fink, M. Halik, H. J. Snaith, C. J. Brabec, *Science.* **2017**, *358* , 1192-1197.

[92] Y. Kim, E. H. Jung, G. Kim, D. Kim, B. J. Kim, J. Seo, *Adv Energy Mater.* **2018**, *8*, 1801668.

[93] N. J. Jeon, H. Na, E. H. Jung, T. Y. Yang, Y. G. Lee, G. Kim, H. W. Shin, S. I. Seok, J. Lee, J. Seo, *Nat Energy.* **2018**, *3*, 682-689.

[94] W. Chen, Y. H. Wu, J. Fan, A. B. Djurisic, F. Z. Liu, H. W. Tam, A. Ng, C. Surya, W. K. Chan, D. Wang, Z. B. He, *Adv Energy Mater.* **2018**, *8*, 1703519.

[95] S. S. Mali, H. J. Kim, S. E. Shim, C. K. Hong, *Nanoscale.* **2016**, *8*, 19189-19194.

[96] Y. Bai, H. N. Chen, S. Xiao, Q. F. Xue, T. Zhang, Z. L. Zhu, Q. Li, C. Hu, Y. Yang, Z. C. Hu, F. Huang, K. S. Wong, H. L. Yip, S. H. Yang, *Adv Funct Mater.* **2016**, *26*, 2950-2958.

[97] W. Chen, Y. C. Zhou, L. J. Wang, Y. H. Wu, B. Tu, B. B. Yu, F. Z. Liu, H. W. Tam, G. Wang, A. B. Djurisic, L. Huang, Z. B. He, *Adv Mater.* **2018**, *30*, 1800515.

[98] Z. Y. Liu, J. J. Chang, Z. H. Lin, L. Zhou, Z. Yang, D. Z. Chen, C. F. Zhang, S. Z. Liu, Y. Hao,*Adv Energy Mater.* **2018**, *8*, 1703432.

[99] J. C. Yu, J. A. Hong, E. D. Jung, D. Bin Kim, S. M. Baek, S. Lee, S. Cho, S. S. Park, K. J. Choi, M. H. Song, *Sci Rep* **2018**, *8*, 1070.

[100] M. Stolterfoht, C. M. Wolff, J. A. Marquez, S. S. Zhang, C. J. Hages, D. Rothhardt, S. Albrecht, P. L. Burn, P. Meredith, T. Unold, D. Neher, *Nat Energy.* **2018**, *3*, 847-854.

[101] J. Peng, J. I. Khan, W. Z. Liu, E. Ugur, T. Duong, Y. L. Wu, H. P. Shen, K. Wang, H. Dang, E. Aydin, X. B. Yang, Y. M. Wan, K. J. Weber, K. R. Catchpole, F. Laquai, S. De Wolf, T. P. White, *Adv Energy Mater.* **2018**, *8*, 1801208.

[102] S. Akin, Y. Altintas, E. Mutlugun, S. Sonmezoglu, *Nano Energy.* **2019**, *60*, 557-566.

[103] S. Akin, *ACS Appl. Mater. Interfaces* **2019**, DOI: 10.1021/acsami.9b13876.

[104] M. Hu, C. Bi, Y. B. Yuan, Y. Bai, J. S. Huang, *Adv Sci.* **2016**, *3*, 1500301.

[105] H. R. Tan, F. L. Che, M. Y. Wei, Y. C. Zhao, M. I. Saidaminov, P. Todorovic, D. Broberg, G. Walters, F. R. Tan, T. T. Zhuang, B. Sun, Z. Q. Liang, H. F. Yuan, E. Fron, J. Kim, Z. Y. Yang, O. Voznyy, M. Asta, E. H. Sargent, *Nat Commun.* **2018**, *9*, 3100.

[106] N. Li, S. Tao, Y. Chen, X. Niu, C. K. Onwudinanti, C. Hu, Z. Qiu, Z. Xu, G. Zheng, L. Wang, Y. Zhang, L. Li, H. Liu, Y. Lun, J. Hong, X. Wang, Y. Liu, H. Xie, Y. Gao, Y. Bai, S. Yang, G. Brocks, Q. Chen, H. Zhou, *Nat. Energy* **2019**, *4*, 408-415.

[107] S. Yang, J. Dai, Z. Yu, Y. Shao, Y. Zhou, X. Xiao, X. C. Zeng, J. Huang, *J Am Chem Soc.* ***2019***, *141*, 5781-5787.

[108] C. Chen, Z. N. Song, C. X. Xiao, D. W. Zhao, N. Shrestha, C. W. Li, G. Yang, F. Yao, X. L. Zheng, R. J. Ellingson, C. S. Jiang, M. Al-Jassim, K. Zhu, G. J. Fang, Y. F. Yan, *Nano Energy.* **2019**, *61*, 141-147.

[109] D. P. McMeekin, G. Sadoughi, W. Rehman, G. E. Eperon, M. Saliba, M. T. Horantner, A. Haghighirad, N. Sakai, L. Korte, B. Rech, M. B. Johnston, L. M. Herz, H. J. Snaith, *Science.* **2016**, *351*, 151-155.

[110] Y. C. Zhao, H. R. Tan, H. F. Yuan, Z. Y. Yang, J. Z. Fan, J. Kim, O. Voznyy, X. W. Gong, L. N. Quan, C. S. Tan, J. Hofkens, D. P. Yu, Q. Zhao, E. H. Sargent, *Nat Commun.* **2018**, *9*, 1607.

[111] K. T. Cho, S. Paek, G. Grancini, C. Roldan-Carmona, P. Gao, Y. H. Lee, M. K. Nazeeruddin, *Energ Environ Sci.* **2017**, *10*, 621-627.

[112] K. Choi, J. Lee, H. I. Kim, C. W. Park, G. W. Kim, H. Choi, S. Park, S. A. Park, T. Park, *Energ Environ Sci.* **2018**, *11* , 3238-3247.

[113] K. Gao, B. Xu, C. S. Hong, X. L. Shi, H. B. Liu, X. S. Li, L. H. Xie, A. K. Y. Jen, *Adv Energy Mater.* **2018**, *8*, 1800809.

[114] N. Chen, Y. Sun, J. J. Peng, W. Zhang, X. J. Su, K. B. Zheng, T. Pullerits, Z. Q. Liang, *Adv Energy Mater.* **2017**, *7*, 1700162.

[115] H. H. Tsai, W. Y. Nie, J. C. Blancon, C. C. S. Toumpos, R. Asadpour, B. Harutyunyan, A. J. Neukirch, R. Verduzco, J. J. Crochet, S. Tretiak, L. Pedesseau, J. Even, M. A. Alam, G. Gupta, J. Lou, P. M. Ajayan, M. J. Bedzyk, M. G. Kanatzidis, A. D. *Nature.* **2016**, *536*, 312-316.

[116] L. Etgar, *Energ Environ Sci.* **2018**, *11*, 234-242.

[117] S. Yang, Y. Wang, P. R. Liu, Y. B. Cheng, H. J. Zhao, H. G. Yang, *Nat Energy.* **2016**, *1*, 15016.

[118] Y. H. Hu, J. Schlipf, M. Wussler, M. L. Petrus, W. Jaegermann, T. Bein, P. Muller-Buschbaum, P. Docampo, *Acs Nano.* **2016**, *10*, 5999-6007.

[119] Z. P. Wang, Q. Q. Lin, F. P. Chmiel, N. Sakai, L. M. Herz, H. J. Snaith, *Nat Energy.* **2017**, *2*, 17135.

[120] E. A. Alharbi, A. Y. Alyamani, D. J. Kubicki, A. R. Uhl, B. J. Walder, A. Q. Alanazi, J. Luo, A. Burgos-Caminal, A. Albadri, H. Albrithen, M. H. Alotaibi, J.-E. Moser, S. M. Zakeeruddin, F. Giordano, L. Emsley, M. Grätzel, *Nat. Commun.* **2019**, *10*, 3008.

[121] J. J. Yoo, S. Wieghold, M. C. Sponseller, M. R. Chua, S. N. Bertram, N. T. P. Hartono, J. S. Tresback, E. C. Hansen, J. P. Correa-Baena, V. Bulovic, T. Buonassisi, S. S. Shin, M. G. Bawendi, *Energ Environ Sci.* **2019**, *12*, 2192-2199.

[122] T. Zhou, H. Lai, T. Liu, D. Lu, X. Wan, X. Zhang, Y. Liu, Y. Chen, *Adv Mater.* **2019**, *31*, 1901242.

[123] G. Grancini, C. Roldan-Carmona, I. Zimmermann, E. Mosconi, X. Lee, D. Martineau, S. Narbey, F. Oswald, F. De Angelis, M. Graetzel, M. K. Nazeeruddin, *Nat Commun.* **2017**, *8*, 15684.

[124] Y. Bai, S. Xiao, C. Hu, T. Zhang, X. Y. Meng, H. Lin, Y. L. Yang, S. H. Yang, *Adv Energy Mater.* **2017**, *7*, 1701038.

[125] D. Y. Luo, W. Q. Yang, Z. P. Wang, A. Sadhanala, Q. Hu, R. Su, R. Shivanna, G. F. Trindade, J. F. Watts, Z. J. Xu, T. H. Liu, K. Chen, F. J. Ye, P. Wu, L. C. Zhao, J. Wu, Y. G. Tu, Y. F. Zhang, X. Y. Yang, W. Zhang, R. H. Friend, Q. H. Gong, H. J. Snaith, R. Zhu, *Science.* **2018**, *360*, 1442-1446.

[126] K. T. Cho, Y. Zhang, S. Orlandi, M. Cavazzini, I. Zimmermann, A. Lesch, N. Tabet, G. Pozzi, G. Grancini, M. K. Nazeeruddin, *Nano Lett.* **2018**, *18*, 5467-5474.

[127] J. W. Lee, Z. H. Dai, T. H. Han, C. Choi, S. Y. Chang, S. J. Lee, N. De Marco, H. X. Zhao, P. Y. Sun, Y. Huang, Y. Yang,*Nat Commun.* **2018**, *9*, 3021.

[128] K. T. Cho, G. Grancini, Y. Lee, E. Oveisi, J. Ryu, O. Almora, M. Tschumi, P. A. Schouwink, G. Seo, S. Heo, J. Park, J. Jang, S. Paek, G. Garcia-Belmonte, M. K. Nazeeruddin, *Energ Environ Sci.* **2018**, *11*, 952-959.

[129] Y. Zhou, F. Wang, Y. Cao, J. P. Wang, H. H. Fang, M. A. Loi, N. Zhao, C. P. Wong, *Adv Energy Mater.* **2017**, *7*, 1701048.

[130] S. Gharibzadeh, B. A. Nejand, M. Jakoby, T. Abzieher, D. Hauschild, S. Moghadamzadeh, J. A. Schwenzer, P. Brenner, R. Schmager, A. A. Haghighirad, L. Weinhardt, U. Lemmer, B. S. Richards, I. A. Howard, U. W. Paetzold, *Adv Energy Mater.* **2019**, *9*, 1803699.

[131] P. Chen, Y. Bai, S. C. Wang, M. Q. Lyu, J. H. Yun, L. Z. Wang, *Adv Funct Mater.* **2018**, *28*, 1706923.

[132] Y. Lin, Y. Bai, Y. J. Fang, Z. L. Chen, S. Yang, X. P. Zheng, S. Tang, Y. Liu, J. J. Zhao, J. S. Huang, *J Phys Chem Lett.* **2018**, *9*, 654-658.

[133] L. Chen, Y. Y. Tan, Z. X. Chen, T. Wang, S. Hu, Z. A. Nan, L. Q. Xie, Y. Hui, J. X. Huang, C. Zhan, S. H. Wang, J. Z. Zhou, J. W. Yan, B. W. Mao, Z. Q. Tian, *J. Am. Chem Soc.* **2019**, *141*, 1665-1671.

[134] S. Bai, P. M. Da, C. Li, Z. P. Wang, Z. C. Yuan, F. Fu, M. Kawecki, X. J. Liu, N. Sakai, J. T. W. Wang, S. Huettner, S. Buecheler, M. Fahlman, F. Gao, H. J. Snaith, *Nature.* **2019**, *571*, 245-250.

[135] S. Yang, S. Chen, E. Mosconi, Y. Fang, X. Xiao, C. Wang, Y. Zhou, Z. Yu, J. Zhao, Y. Gao, F. De Angelis, J. Huang, *Science* **2019**, *365*, 473-478.

[136] Y. Wang, T. Wu, J. Barbaud, W. Kong, D. Cui, H. Chen, X. Yang, L. Han, *Science* **2019**, *365*, 687-691.

[137] P. Qin, S. Tanaka, S. Ito, N. Tetreault, K. Manabe, H. Nishino, M. K. Nazeeruddin, M. Gratzel, *Nat Commun.* **2014**, *5*, 3834.

[138] L. Kavan, Z. V. Zivcova, P. Hubik, N. Arora, M. I. Dar, S. M. Zakeeruddin, M. Gratzel, *ACS Appl. Energy Mater.* **2019**, *2*, 4264-4273.

[139] N. Arora, M. I. Dar, A. Hinderhofer, N. Pellet, F. Schreiber, S. M. Zakeeruddin, M. Gratzel, *Science.* **2017**, *358*, 768-771.

[140] J. V. Milic, N. Arora, M. I. Dar, S. M. Zakeeruddin, M. Gratzel, *Adv. Mater Interfaces.* **2018**, *5*, 1800416.

[141] N. Arora, M. I. Dar, S. Akin, R. Uchida, T. Baumeler, Y. Liu, S. M. Zakeeruddin, M. Gratzel *Small*, **2019**, DOI: 10.1002/smll.201904746.

[142] L. Wang, H. Zhou, J. Hu, B. Huang, M. Sun, B. Dong, G. Zheng, Y. Huang, Y. Chen, L. Li, Z. Xu, N. Li, Z. Liu, Q. Chen, L.-D. Sun, C.-H. Yan, *Science* **2019**, *363*, 265-270.

[143] S. G. Hashmi, D. Martineau, X. Li, M. Ozkan, A. Tiihonen, M. I. Dar, T. Sarikka, S. M. Zakeeruddin, J. Paltakari, P. D. Lund, M. Grätzel, *Adv. Mater. Technol.* **2017**, *2*, 1600183.

[144] S. G. Hashmi, D. Martineau, M. I. Dar, T. T. T. Myllymäki, T. Sarikka, V. Ulla, S. M. Zakeeruddin, M. Grätzel, *J. Mater. Chem. A* **2017**, *5*, 12060-12067.

[145] D. Di Girolamo, M. I. Dar, D. Dini, L. Gontrani, R. Caminiti, A. Mattoni, M. Graetzel, S. Meloni, *J. Mater. Chem. A* **2019**, *7*, 12292-12302.

[146] Y. Hou, Z. R. Zhou, T. Y. Wen, H. W. Qiao, Z. Q. Lin, B. Ge, H. G. Yang, *Nanoscale Horiz.* **2019**, *4*, 208-213.

[147] L. L. Gao, I. Spanopoulos, W. J. Ke, S. Huang, I. Hadar, L. Chen, X. L. Li, G. J. Yang, M. G. Kanatzidis, *Acs Energy Lett.* **2019**, *4*, 1763-1769.

[148] Y. F. Yue, N. Salim, Y. Z. Wu, X. D. Yang, A. Islam, W. Chen, J. Liu, E. B. Bi, F. X. Xie, M. L. Cai, L. Y. Han, *Adv Mater.* **2016**, *28*, 10738-10743.

[149] D. D. Song, D. Wei, P. Cui, M. C. Li, Z. Q. Duan, T. Y. Wang, J. Ji, Y. Y. Li, J. M. Mbengue, Y. F. Li, Y. He, M. Trevor, N. G. Park, *J Mater Chem A.* **2016**, *4*, 6091-6097.

[150] J. B. Zhang, B. Xu, L. Yang, A. Mingorance, C. Q. Ruan, Y. Hua, L. Q. Wang, N. Vlachopoulos, M. Lira-Cantu, G. Boschloo, A. Hagfeldt, L. C. Sun, E. M. J. Johansson, *Adv Energy Mater.* **2017**, *7*, 1602736.

[151] L. Calio, M. Salado, S. Kazim, S. Ahmad, *Joule.* **2018**, *2*, 1800-1815.

[152] I. Jeon, H. Ueno, S. Seo, K. Aitola, R. Nishikubo, A. Saeki, H. Okada, G. Boschloo, S. Maruyama, Y. Matsuo, *Angew. Chem., Int. Ed.*. **2018**, *57*, 4607-4611.

[153] W. Luo, C. C. Wu, D. Wang, Y. Q. Zhang, Z. H. Zhang, X. Qi, N. Zhu, X. Guo, B. Qu, L. X. Xiao, Z. J. Chen, *Acs Appl Mater Inter.* **2019**, *11*, 9149-9155.

[154] F. Bella, G. Griffini, J. P. Correa-Baena, G. Saracco, M. Gratzel, A. Hagfeldt, S. Turri, C. Gerbaldi, *Science.* **2016**, *354*, 203-206.

Michael Graetzel is a Professor at the Ecole Polytechnique Fédérale de Lausanne (EPFL). He directs there the Laboratory of Photonics and Interfaces. He pioneered research on energy and electron transfer reactions in mesoscopic systems and their use to generate electricity and fuels from sunlight. He is credited with moving the solar cell field beyond the principle of light absorption via diodes to the molecular level exploiting the sensitization of 3D nanoparticle networks of semiconductors oxides by dyes, pigments, or quantum dots for light energy harvesting.

Richard Friend holds the Cavendish Professorship of Physics at the University of Cambridge. His research encompasses the physics, materials science and engineering of semiconductor devices made with carbon-based semiconductors, particularly polymers. His research advances have shown that carbon-based semiconductors have significant applications in light-emitting devices, solar cells, lasers, and electronics. These have been developed and exploited through a number of spin-off companies. His current research interests are directed to novel schemes to improve the performance and cost of solar cells.

M. Ibrahim Dar is an Advanced Swiss National Science Foundation Fellow working in collaboration with Prof. Sir Richard Friend at the Cavendish Laboratory, the University of

Cambridge. From 2014-2018, he worked as a Post-Doctoral Scientist with Prof. Michael Graetzel at EPFL, Switzerland. He received his PhD in Nanoscience at Indian Institute of Science, Bangalore, India in 2014. During this period, he was also awarded the Swiss Government Excellence Research Scholarship to work as a guest PhD scholar in Prof. Graetzel group at EPFL. His current research focuses on understanding structural, compositional and optoelectronic properties of materials for their application in light-harnessing and light-emitting devices.

The table of contents entry

Despite the record efficiency exceeding 25%, the long-term operational stability of perovskite solar cells is limited by the degradation mechanisims accelerated by the presence of vacancies and defects. In this review, recent engineering strategies ranging from grains to interfaces that mitigate degradation and improve efficincies are discussed.

Keyword (perovskite solar cells, defects, passivation, efficiency, mixed-cation-halide, 2D-3D, engineering, stability)

Seckin Akin, Neha Arora*, Shaik M. Zakeeruddin, Michael Grätzel, Richard H. Friend, M. Ibrahim Dar*

New Passivation Strategies for High-Efficiency and Stable Perovskite Solar Cells